AD-A101 728 ENVIRONMENTAL RESEARCH INST OF MICHIGAN ANN ARBOR RA--ETC F/G 5/8
FOURIER MODULUS IMAGE CONSTRUCTION.(U)
MAY 81 J E FIENUP F30602-80-C-0002
UNCLASSIFIED RADC-TR-81-63 NL

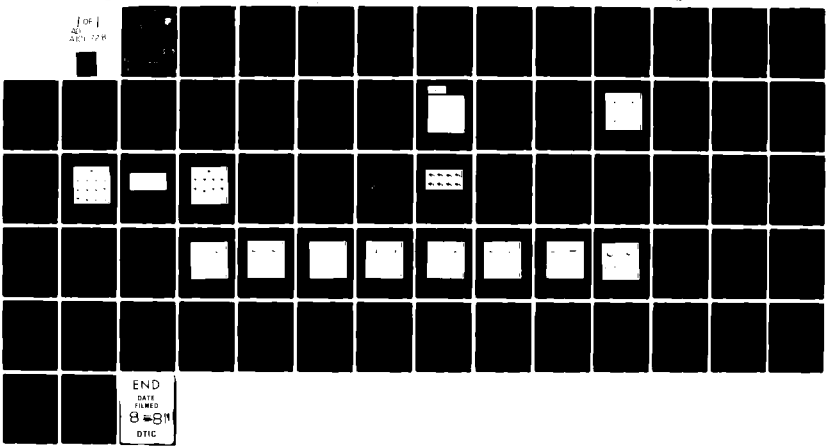

LEVEL II

RADC-TR-81-63
Final Technical Report
May 1981

AD A101728

FOURIER MODULUS IMAGE CONSTRUCTION

Environmental Research Institute of Michigan

James R. Fienup

APPROVED FOR PUBLIC RELEASE; DISTRIBUTION UNLIMITED

DTIC
ELECTE
JUL 22 1981
S D
D

This effort was funded totally by the Laboratory Directors' Fund.

DTIC FILE COPY

ROME AIR DEVELOPMENT CENTER
Air Force Systems Command
Griffiss Air Force Base, New York 13441

81 7 22 004

This report has been reviewed by the RADC Public Affairs Office (PA) and is releasable to the National Technical Information Service (NTIS). At NTIS it will be releasable to the general public, including foreign nations.

RADC-TR-81-63 has been reviewed and is approved for publication.

APPROVED: Donald W. Hanson

DONALD W. HANSON
Project Engineer

APPROVED: Frank J. Rehm

FRANK J. REHM
Technical Director
Surveillance Division

FOR THE COMMANDER: John P. Huss

JOHN P. HUSS
Acting Chief, Plans Office

If your address has changed or if you wish to be removed from the RADC mailing list, or if the addressee is no longer employed by your organization, please notify RADC (OCSE) Griffiss AFB NY 13441. This will assist us in maintaining a current mailing list.

Do not return this copy. Retain or destroy.

MISSION
of
Rome Air Development Center

RADC plans and executes research, development, test and selected acquisition programs in support of Command, Control Communications and Intelligence (C^3I) activities. Technical and engineering support within areas of technical competence is provided to ESD Program Offices (POs) and other ESD elements. The principal technical mission areas are communications, electromagnetic guidance and control, surveillance of ground and aerospace objects, intelligence data collection and handling, information system technology, ionospheric propagation, solid state sciences, microwave physics and electronic reliability, maintainability and compatibility.

UNCLASSIFIED

SECURITY CLASSIFICATION OF THIS PAGE (When Data Entered)

REPORT DOCUMENTATION PAGE

READ INSTRUCTIONS BEFORE COMPLETING FORM

1. REPORT NUMBER: RADC-TR-81-63

2. GOVT ACCESSION NO.: AD-A101728

3. RECIPIENT'S CATALOG NUMBER:

4. TITLE (and Subtitle): FOURIER MODULUS IMAGE CONSTRUCTION

5. TYPE OF REPORT & PERIOD COVERED: Final Technical Report, 7 Sep 79 – 30 Sep 80

6. PERFORMING ORG. REPORT NUMBER: N/A

7. AUTHOR(s): James E. Fienup

8. CONTRACT OR GRANT NUMBER(s): F30602-80-C-0002

9. PERFORMING ORGANIZATION NAME AND ADDRESS: Environmental Research Institute of Michigan, Radar and Optics Division, P. O. Box 8618, Ann Arbor MI 48107

10. PROGRAM ELEMENT, PROJECT, TASK AREA & WORK UNIT NUMBERS: 61101F, LD001C1

11. CONTROLLING OFFICE NAME AND ADDRESS: Rome Air Development Center (OCSE), Griffiss AFB NY 13441

12. REPORT DATE: May 1981

13. NUMBER OF PAGES: 69

14. MONITORING AGENCY NAME & ADDRESS (if different from Controlling Office): Same

15. SECURITY CLASS. (of this report): UNCLASSIFIED

15a. DECLASSIFICATION/DOWNGRADING SCHEDULE: N/A

16. DISTRIBUTION STATEMENT (of this Report):

Approved for public release; distribution unlimited.

17. DISTRIBUTION STATEMENT (of the abstract entered in Block 20, if different from Report):

Same

18. SUPPLEMENTARY NOTES

RADC Project Engineer: Donald W. Hanson (OCSE)

This effort was funded totally by the Laboratory Directors' Fund.

19. KEY WORDS (Continue on reverse side if necessary and identify by block number)

Speckly Interferometry
Turbulence
Ambiguity
Uniqueness
Iterative Algorithm
Image Processing

20. ABSTRACT (Continue on reverse side if necessary and identify by block number)

This report describes the investigation of a new method for recovering diffraction-limited images through the turbulent atmosphere. ~~The method~~ consists of an iterative algorithm that constructs an image from Fourier modulus data which is measured by stellar speckly interferometry. The results of this research indicate that the method has the potential for providing diffraction-limited images of earth-orbiting satellites.

DD FORM 1 JAN 73 1473 EDITION OF 1 NOV 65 IS OBSOLETE

UNCLASSIFIED

SECURITY CLASSIFICATION OF THIS PAGE (When Data Entered)

Image construction experiments were performed on Fourier modulus data computer-simulated to include the effects of atmospheric turbulence, diffraction, photon (Poisson statistics) noise, and a finite number of short-exposure images. The quality of the constructed images was found to degrade in a gradual and predictable manner as the signal-to-noise ratio decreases. The rms error of the constructed images was found to vary approximately as the square root of the rms error of the Fourier modulus data. Diffraction-limited images were constructed for levels of photon noise that would be expected for imaging satellites through a 1.6-meter telescope.

Image construction experiments were performed on the Fourier modulus of a number of different objects of varying complexity. Interpretation of the results was complicated by a tendency of the algorithm to stagnate at local minimum having the appearance of a good quality image superimposed by a pattern of stripes. Nevertheless, the results were suggestive that the solution is usually unique; only for an object satisfying special conditions is the Fourier modulus ambiguous. As the signal-to-noise ratio decreases, the ambiguity of the solution increases, but that ambiguity takes the form of noise in the constructed image rather than a complete change in the basic shape of the image.

Several variations of the algorithm were compared, and one was found to converge considerably faster than the others. The convergence time was longer for objects of greater complexity. For an array size of 128 x 128 pixels, typically one hundred iterations are required, taking about two minutes on an array processor.

PREFACE

This report was prepared by the Electro-Optics Department of the Radar and Optics Division of the Environmental Research Institute of Michigan. The work was sponsored by AFSC, Rome Air Development Center, under Contract No. F30602-80-C-0002.

This final technical report covers work performed between 7 September 1979 and 30 September 1980. The project engineer is Donald W. Hanson, Rome Air Development Center/OCSE, Griffiss AFB, New York 13441. The principal investigator is James R. Fienup. Major contibutors to the effort are Gerald B. Feldkamp and James R. Fienup. Acknowledgment is due to David L. Fried (the Optical Sciences Co.) and Benjamin L. McGlamery (Visibility Labs., Scripps Institution of Oceanography) for helpful discussions and to McGlamery for supplying ERIM with digital image data.

Accession For
NTIS GRA&I ☒
DTIC TAB ☐
Unannounced ☐
Justification
By
Distribution/
Availability Codes
Dist | Avail and/or Special
A

SUMMARY

This report describes the investigation of a new method for recovering diffraction-limited images through the turbulent atmosphere. The method consists of an iterative algorithm that constructs an image from Fourier modulus data which is measured by stellar speckle interferometry. The results of this research indicate that the method has the potential for providing diffraction-limited images of earth-orbiting satellites.

Image construction experiments were performed on Fourier modulus data computer-simulated to include the effects of atmospheric turbulence, diffraction, photon (Poisson statistics) noise, and a finite number of short-exposure images. The quality of the constructed images was found to degrade in a gradual and predictable manner as the signal-to-noise ratio decreases. The rms error of the constructed images was found to vary approximately as the square root of the rms error of the Fourier modulus data. Diffraction-limited images were constructed for levels of photon noise that would be expected for imaging satellites through a 1.6-meter telescope.

Image construction experiments were peformed on the Fourier modulus of a number of different objects of varying complexity. Interpretation of the results was complicated by a tendency of the algorithm to stagnate at local minimum having the appearance of a good quality image superimposed by a pattern of stripes. Nevertheless, the results were suggestive that the solution is usually unique; only for an object satisfying special conditions is the Fourier modulus ambiguous. As the signal-to-noise ratio decreases, the ambiguity of the solution increases, but that ambiguity takes the form of noise in the constructed image rather than a complete change in the basic shape of the image.

Several variations of the algorithm were compared, and one was found to converge considerably faster than the others. The convergence time was longer for objects of greater complexity. For an array size of 128 x 128 pixels, typically one hundred iterations are required, taking about two minutes on an array processor.

CONTENTS

Preface 3

Summary..... 4

List of Illustrations..... 6

List of Tables..... 7

1. Introduction..... 9

2. Iterative Method Background..... 10

3. Noise Properties of Images Constructed from Fourier Modulus..... 16

   3.1 Simulation of Noisy Fourier Modulus Data 16
   3.2 Image Construction Results from Noisy Fourier Modulus 23

4. Uniqueness of Images Constructed from Fourier Modulus..... 34

   4.1 Uniqueness Theory 34
   4.2 Uniqueness Experiments 36

5. Algorithm Convergence..... 49

   5.1 Comparison of Different Algorithms 49
   5.2 Data Dependency of Convergence 54
   5.3 The Stripes Phenomenon 55

6. Conclusions and Recommendations for Future Research.... 57

Appendix A. Convergence Proof..... 61

References..... 66

LIST OF ILLUSTRATIONS

1. (A) Block diagram of the Iterative Method; (B) the Input-Output Concept for the Iterative Method.....11

2. The Reference Object.....17

3. Degraded Images.....17

4. Fourier Modulus Estimates Computed from 156 Degraded Images Each.....20

5. Rms Error of Fourier Modulus Estimate, $E_{|\hat{F}|}$, vs. Number of Photons per Degraded Image, $N_c/156$.....22

6. (A) Reference Object; (B)-(M) Images Constructed from Fourier Modulus Estimates, Corresponding to the Data Points in Figure 5 for the High Resolution Case, Excluding the Lowest Noise Case.....25

   (N)-(U) Photon-Limited Short-Exposure Images with No Atmosphere Present.....26

7. (A) Low Resolution Version of Reference Object; (B)-(I) Images Constructed from Low Resolution Versions of the Fourier Modulus Estimates, Corresponding to the Data Points in the Lower Curve of Figure 5.....27

8. Rms Error of Constructed Images, $\tilde{E}$, Versus rms Error of the Fourier Modulus Estimates, $E_{|\hat{F}|}$..... 30

9. Four Images Constructed Using Different Starting Inputs..... 31

10. Reference Objects and Constructed Images for Film No. 204, P72-2(A)..... 41

11. Reference Objects and Constructed Images for Film No. 205, P72-2(B)..... 42

12. Reference Objects and Constructed Images for Film No. 302, 777(A)..... 43

13. Reference Objects and Constructed Images for Film No. 314, 777(B)..... 44

14. Reference Objects and Constructed Images for Film No. 401, FLTSATCOM..... 45

15. Reference Objects and Constructed Images for Film No. 509, LST(A)..... 46

16. Reference Objects and Constructed Images for Film No. 508, LST(B)..... 47

LIST OF ILLUSTRATIONS
(Continued)

17. Reference Objects and Constructed Images for Film No. 608, SURVSATCOM.....48

18. Rms Error, E_0, After Sequence of 20 Iterations Versus Algorithm Parameter β for the Basic Input-Output Approach (Δ), the Output-Output Approach ($\bullet$) and the Hybrid Input-Output Approach(x).....53

A1. Fourier Domain Quantities for a Given Value of (p, q), Showing that $|N_{k+1,pq}| \leq |D_{k,\ pq}|$..... 64

LIST OF TABLES

1. Objects for Uniqueness Study.....40

2. Rms Error E_0 of Construction Results for Uniqueness Study..... 40

BLANK PAGE

FOURIER MODULUS IMAGE CONSTRUCTION

1
INTRODUCTION

The purpose of this research project is to investigate the effectiveness of a new method of recovering fine resolution imagery through the turbulent atmosphere.

Ordinarily, atmospheric turbulence limits the resolution of an image obtained through a large optical telescope to about one second of arc at best, which corresponds to the diffraction limit of an optical telescope of aperture 10 cm. By comparison, the theoretical diffraction-limited resolution of a 2-meter telescope with no atmospheric turbulence is 0.05 arc-seconds -- 20 times finer. Compensated imaging (real-time correction of atmospheric turbulence-induced phase errors by adaptive optics) can produce diffraction-limited images, but the system is expensive. An inexpensive alternative approach is to gather fine resolution information by stellar speckle interferometry [1], and then process that information to form an image. The information obtained from speckle interferometry is the modulus of the object's Fourier transform, or equivalently the autocorrelation of the object. An image can be constructed from this information using an iterative algorithm [2]. The imagery thus obtained would have diffraction-limited resolution.

This research project had three major goals: (1) to determine how the quality of the constructed images varied with the signal-to-noise ratio of the Fourier modulus data; (2) to determine whether the algorithm could produce spurious results (that is, whether the constructed image is unique); and (3) to investigate changes in the algorithm to improve convergence of the algorithm and to determine how the convergence time varies with the properties of the Fourier modulus data. Section 2 of this report gives background to the iterative algorithm. Sections 3 through 5, respectively, describe the results relating to the three goals listed above. Section 6 summarizes the conclusions and outlines areas where further work is needed. Appendix A contains a proof of convergence for one version of the iterative algorithm.

2
ITERATIVE METHOD BACKGROUND

This section briefly describes the iterative method, which is discussed in more detail elsewhere [2, 3] and in Section 5. Since the experiments were performed on a digital computer, the object and its Fourier transform are sampled functions. Throughout this report, the convention is used that functions represented by upper case letters are the Fourier transforms of functions represented by lower case letters.

Let the object distribution be f_{mn} and its discrete Fourier transform be

$$F_{pq} = |F_{pq}| \exp(i\theta_{pq}) = \mathcal{F}[f_{mn}] = \sum_{mn} f_{mn} \exp[-j(2\pi/N)(mp + nq)] \quad (1)$$

where m, n, p, and q = 0, 1, 2, . . ., N - 1. m and n are referred to as spatial coordinates and p and q as spatial frequency coordinates. The object brightness distribution f_{mn} is real and nonnegative and F_{pq} is Hermitian. We assume that only $|F_{pq}|$ is measured, although in some cases of practical interest θ_{pq} may be measurable for very low spatial frequencies. The diameter of the object can be computed since it is half the diameter of the autocorrelation $f \star f = \mathcal{F}^{-1}[|F_{pq}|^2]$. The problem is to reconstruct the object f_{mn}, or equivalently the phase θ_{pq}, from $|F_{pq}|$ consistent with the fact that $f_{mn} \geq 0$. Use of the constraint of the object's computed diameter is not essential, since any nonnegative solution having a Fourier modulus $|F_{pq}|$ automatically has the correct diameter.

A block diagram of the iterative method is depicted in Figure 1a. The four steps of each iteration are as follows. (1) An input image g_{mn} (which in some instances may be considered an estimate of the object) is Fourier transformed:

$$G_{pq} = |G_{pq}| \exp(i\phi_{pq}) = \mathcal{F}[g_{mn}]$$

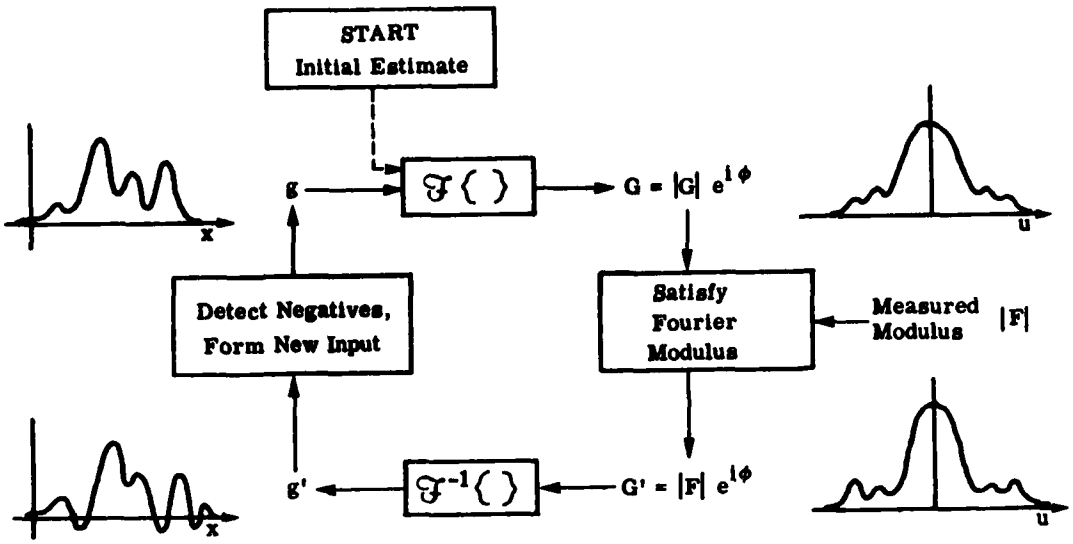

(A)

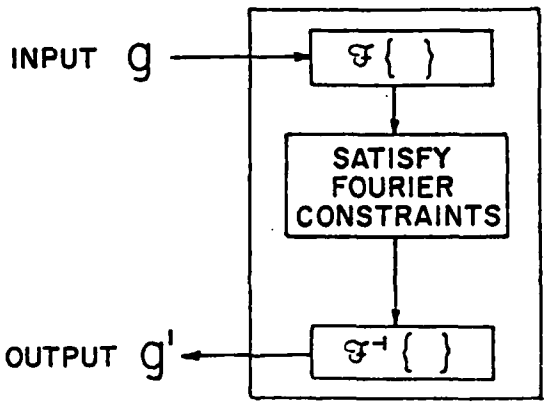

(B)

Figure 1. (A) Block diagram of the iterative method; (B) the input-output concept for the iterative method.

(2) The result is made to satisfy the measured Fourier modulus and the computed phase is left unchanged:

$$G'_{pq} = |F_{pq}| \exp(i\phi_{pq})$$

(3) The result is inverse Fourier transform:

$$g'_{mn} = \mathcal{F}^{-1} [G'_{pq}]$$

(4) Based on how g'_{mn} violates the object-domain constraints, a new input g_{mn} is formed, and the process is repeated.

Taken together as a group, the first three steps can be viewed as a nonlinear system having an input g_{mn} and an output g'_{mn} as depicted in Figure 1b. The output g'_{mn} is guaranteed to have a Fourier transform with the measured modulus. Therefore, if g'_{mn} is nonnegative, then it is a solution to the problem; that is, it simultaneously agrees with the measured data in the Fourier domain and the a priori nonnegativity constraint in the image (or object) domain. The procedure is to iteratively change the input in such a way as to drive the output to be everywhere nonnegative. Driving the output to be zero outside the computed diameter may also be included; imposition of the diameter constraint is not essential, but it decreases the convergence time of the algorithm.

The iterative method embraces a family of algorithms for altering the input in order to drive the output to satisfy the object-domain constraints. Two such methods of altering the input that were used for the experiments reported here are given by

$$g_{k+1,mn} = \begin{cases} g'_{k,mn}, & (m,n) \notin \gamma \\ 0, & (m,n) \in \gamma \end{cases} \tag{2}$$

and

$$g_{k+1,mn} = \begin{cases} g'_{k,mn}, & (m,n) \notin \gamma \\ g_{k,mn} - \beta g'_{k,mn}, & (m,n) \in \gamma \end{cases} \tag{3}$$

where $g_{k,mn}$ and $g'_{k,mn}$ are the input and output, respectively, at the kth iteration, γ is the set of points at which $g'_{k,mn}$ violates the constraints, and β is a constant. We refer to the iterative method using Eq. (2) as the error-reduction approach, since it can be shown that the mean-squared error defined in the Fourier domain by

$$E_F^2 = \frac{\sum_{pq}\left(\left|G_{pq}\right| - \left|F_{pq}\right|^2\right)}{\sum_{pq} F_{pq}^{\ 2}} \tag{4}$$

or in the image domain by

$$E_o^2 = \frac{\sum_{mn\epsilon\gamma} \left|g'_{mn}\right|^2}{\sum_{mn} \left|g'_{mn}\right|^2} \tag{5}$$

can only decrease at each iteration. The proof of convergence is given in Appendix A. These two error measures indicate the degree to which the solution agrees with the measured Fourier modulus. Unfortunately, the fractional decrease of the error becomes very small as the iterations progress, and the error-reduction approach usually does not converge to a solution in a practical sense.

An important notion that is used in Eq. (3) and other related methods of altering the input is that a change of the input tends to result in a similar (but somewhat different) change of the output [4]. We refer to these methods of altering the input as the input-output approach. Although the mean-squared error does not necessarily decrease at each iteration (it may even increase), in practice the input-output approach converges much faster than the error-reduction approach. The optimum choice of the constant β in Eq. (3) depends on the statistics of G_{pq} and F_{pq}. We have found values of β between 0.5 and 1.0 to work well. The input-output approach can be used by itself, or it can be alternated with the error-reduction approach. For the results shown in Sections 3 and 4, we alternated between Eq. (2) and Eq. (3), typically performing thirty to sixty iterations using Eq. (3) followed by ten iterations using Eq. (2).

The region γ in Eqs. (2) and (3) includes all points at which $g'_{k,mn}$ violates the object-domain constraints. The primary constraint is that the image be nonnegative. Another constraint that may be imposed is that the diameter of the image not exceed half the diameter of the autocorrelation. For the set of experiments described in Sections 3 and 4, we applied a tight diameter constraint for the first few iterations, but only constrained the image to half the field-of-view (and the images always fit within less than half the field-of-view) in each dimension for the bulk of the iterations.

As mentioned earlier, the diameter constraint is not essential, since all real, nonnegative solutions automatically have the correct diameter (half the diameter of the autocorrelation). However, during the iterations the intermediate results (the output images g') do have a diameter exceeding the known diameter, and by applying the diameter constraint the convergence time of the algorithm is decreased. That g' can have a diameter greater than half the diameter of the autocorrelation can be seen from the following example. Suppose that for a given iteration the input g is nonnegative and has the correct diameter, but has an incorrect Fourier modulus. After Fourier transformation, its Fourier transform G is modified to satisfy the measured Fourier modulus, $|F|$, which we will assume is exactly the Fourier modulus of the object. Neglecting the case where $|G| = 0$ (it is almost never exactly equal to zero, due to noise, etc), this can be accomplished by multiplying G by $|F|/|G|$,

$$G'_{pq} = G_{pq}\left(\frac{|F_{pq}|}{|G_{pq}|}\right)$$

By the convolution theorem the resulting output image can be expressed as

$$g'_{mn} = g_{mn} * \mathcal{F}^{-1}\left[\frac{|F_{pq}|}{|G_{pq}|}\right]$$

In general the Fourier transform of $(|F|/|G|)$ will have positive and negative sidelobes that extend over the entire field-of-view. Therefore g' will contain areas of positive and negative values that extend beyond half the diameter of the autocorrelation. Nevertheless g' and the object must have

identical autocorrelations: since $|G'| = |F|$, $g' \bigstar g' = \mathcal{F}^{-1}[|G'|^2] = \mathcal{F}^{-1}[|F|^2] = f \bigstar f$. The diameter of g' can exceed half the diameter of the autocorrelation only if g' has regions of negative value, since negative values are required to get the cancellation needed to reduce the diameter of the autocorrelation to less than twice the diameter of g'.

3
NOISE PROPERTIES OF IMAGES CONSTRUCTED FROM FOURIER MODULUS

This section describes a set of experiments aimed at determining how the quality of the constructed images depends on the amount of noise present in the ·ured Fourier modulus data. Noisy Fourier modulus data was simulated having predetermined amounts of noise, images were constructed from the noisy Fourier modulus data, and a measure was made of the quality of the constructed images.

3.1 SIMULATION OF NOISY FOURIER MODULUS DATA

The Fourier modulus data used for the reconstruction experiments was simulated to include the effects of atmospheric turbulence and photon noise. The object used (a digitized photograph of a P72-2 sensor testbed) is shown in Figure 2, as it would appear through a diffraction-limited telescope with no atmospheric turbulence and no noise. The object is about 64 x 40 pixels in extent, imbedded in a 128 x 128 array. The object f_{mn} was convolved with 156 different point-spread functions (PSFs) to produce 156 different blurred images

$$d_{mn}^{(k)} = f_{mn} * s_{mn}^{(k)} = \mathcal{F}^{-1}\left[F_{pq}\, S_{pq}^{(k)}\right],\ k = 1, \ldots, 156 \quad (6)$$

where $s_{mn}^{(k)}$ is the kth PSF. The object and the PSFs were supplied by B. L. McGlamery (Visibility Laboratory, Scripps Institution of Oceanography, U.C. San Diego) and were computed from phase functions representing the effects of a model of atmospheric turbulence having a Kolmogorov spectrum [5], assuming a telescope lens diameter of 1.6 meters and r_0 (Fried's parameter [6]) = 0.1 meters. Examples of the blurred images $d_{mn}^{(k)}$ are shown in Figure 3(a)-(d). The blurred images were then converted to mean photon counts and subjected to a Poisson noise process: each pixel was replaced with a sample drawn from a Poisson distribution with mean and variance equal to the mean photon count, resulting in the noisy degraded images $i_{mn}^{(k)}$.

A point of reference for the amount of photon noise present in the data is given by an analysis done by B. L. McGlamery [7]. He assumed that the

Figure 2. The reference object.

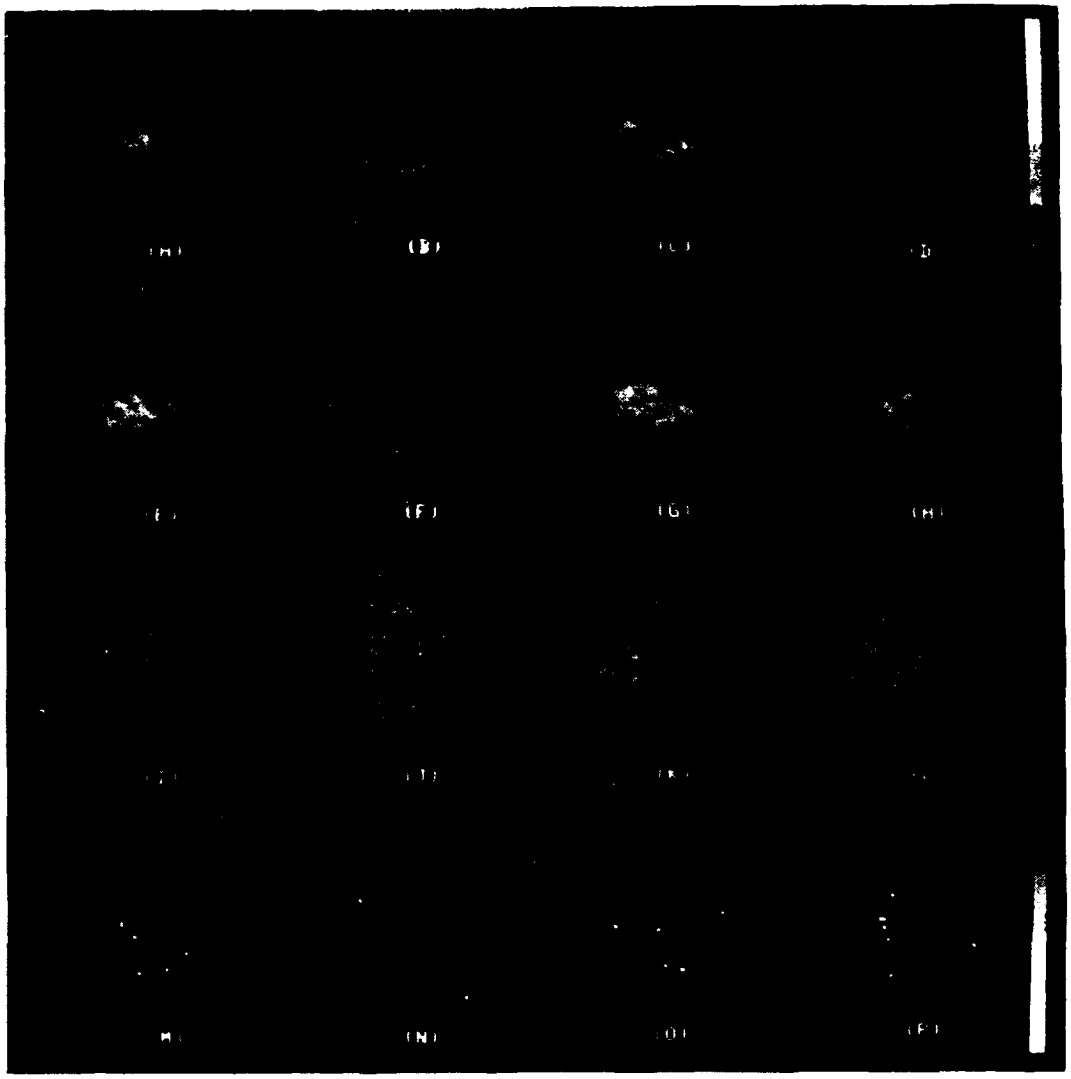

Figure 3. Degraded images. (A)-(D) Noise-free blurred images; degraded (blurred and noisy) images—number of photons per degraded images: (E)-(H) 305,000; (I)-(L) 6143; (M)-(P) 643.

short-exposure blurred images were obtained with a system having the following parameters:

1.6 m	=	telescope diameter
5 msec	=	exposure time
100 nm	=	spectral bandwidth
550 nm	=	center wavelength
0.8	=	atmospheric transmittance

and assuming a 5900°K spectral curve for the solar irradiance, and an S20 sensor spectral sensitivity curve. For the P72-2 object (Figure 2) at a magnification equivalent to a distance of 300 km, the blurred images (reflectance maps) were multiplied by a constant of value 2779 to convert the image to a mean value of photoelectrons/pixels (mean photon counts). We refer to this constant for converting reflectance into mean photoelectrons as the photoelectron scale factor. The value of 2779 pertains to the system and exposure time described above, which was considered to be realistic for observing satellites (although the spectral bandwidth of 100 nm may be considered to be too high by as much as a factor of two). Using 156 blurred images, this case serves as a baseline. For other cases there would be greater or fewer photons available according to the reflectivity of the object and the values of the parameters listed above. The net effect on the photon noise of all of these factors was simulated by lumping them all into one number, the photoelectron scale factor. For our experiments the photoelectron scale factor was varied between 6 and 55580 which is equivalent to between 0.002 times and 20 times the number of photons for the baseline case. The values of the photoelectron scale factor that were used are 55580, 27790, 13895, 5558, 2779, 1390, 556, 278, 139, 56, 28, 14, and 6.

Examples of the noisy, degraded images, including both the blurring due to the atmosphere (and the telescope aperture) and photon noise, are shown in Figure 3.

This simulated speckle data was then processed by the Labeyrie method [1], as modified by Goodman and Belsher [8] and later by others [9], to arrive at an estimate of the modulus of the Fourier transform of the object:

$$|\hat{F}_{pq}| = W_{pq}\left[\frac{\sum_{k=1}^{156} |I_{pq}^{(k)}|^2 - N_c}{\sum_{k=1}^{156} |S_{pq}^{(k)}|^2}\right]^{1/2} \tag{7}$$

where

$$N_c = \sum_k \sum_{mn} i_{mn}^{(k)} = \sum_k I_{oo}^{(k)} \tag{8}$$

is a constant equal to the total number of photons detected [8, 9], $\sum |S_{pq}^{(k)}|^2$ is the square of the MTF of the speckle interferometry process, and W_{pq} is a weighting factor. Examples of $|\hat{F}_{pq}|$ are shown in Figure 4. The subtraction of N_c eliminates one particular constant noise term due to photon statistics. Other noise terms remain. If the sensor is operating in a photon-counting mode, then N_c can be calculated from Eq. (8) as it was for our experiments; otherwise, N_c can be estimated as the minimum value of $\sum |I_{pq}^{(k)}|^2$ at high spatial frequencies. In a real-world situation, it may also be necessary to compensate for the MTF due to the detection process before subtracting N_c [10]. In the real world an estimate of the MTF in the denominator of Eq. (7) can be obtained from measurements on an unresolved star or determined from a model of the atmosphere. For this experiment the intent was to separate out the effects due to photon noise alone, so the exact MTF was used. Division by the MTF also compensates for the MTF due to the telescope aperture, resulting in a net system transfer function that is unity within a circle of radius equal to twice the radius of the telescope aperture, and is set to zero outside that aperture. The result would be a system impulse response having undesirable negative sidelobes. The weighting function W_{pq} was included in Eq. (7) in order to restore the natural MTF associated with a telescope having a circular aperture (that MTF being the autocorrelation of the circular aperture), and the resulting system impulse response no longer has negative sidelobes. The undegraded image shown in Figure 2, which we refer to as the reference object, was also subjected to the same weighting function in the Fourier domain to impose on it the transfer function of the telescope aperture. The radius of

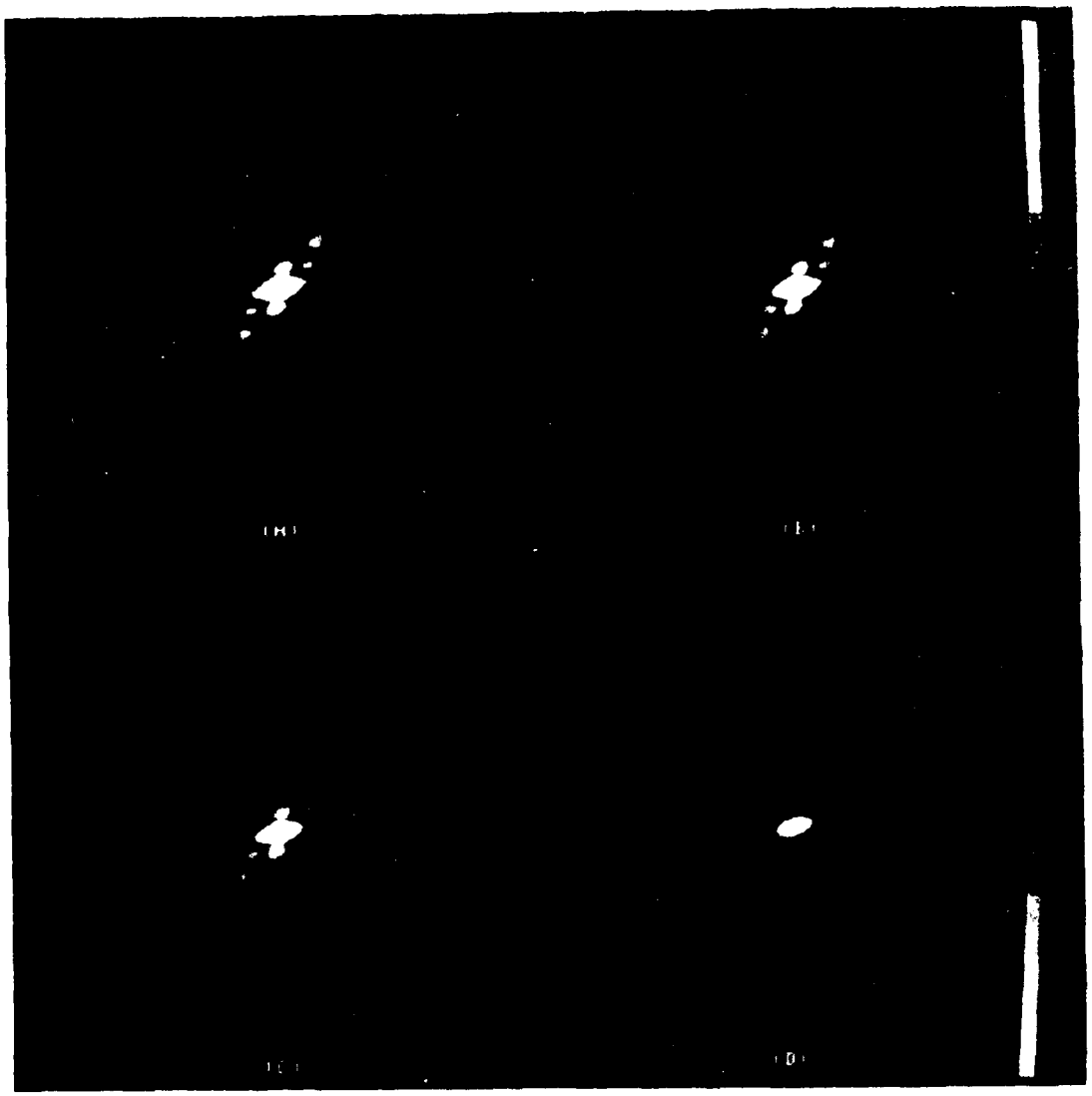

Figure 4. Fourier modulus estimates computed from 156 degraded images each. Number of photons per degraded image: (A) infinity (noise-free); (B) 305,000; (C) 6143; (D) 643.

W_{pq} was 62 pixels, corresponding to the MTF of a telescope of diameter 1.6 meters.

An indication of the signal-to-noise ratio of the Fourier modulus estimate $|\hat{F}_{pq}|$ can be obtained from the total number of photons detected, N_c. Values of N_c for the Fourier modulus estimates were varied from 9.5 x 10^8 for the lowest noise case (photoelectron scale factor = 55580) to 1.0 x 10^5 for the highest noise case (photoelectron scale factor = 6). Since 156 degraded images were used to compute the Fourier modulus estimates, this corresponds to a range of 6.1 x 10^6 to 643 photons per degraded image. Since each blurred image extended over an area of about 64 by 64 pixels, this corresponds to a range of 1490 to 0.16 photons per pixel per degraded image over the area of the degraded image. For the baseline case having a photoelectron scale factor of 2779, the value of N_c was 4.7 x 10^7, which is equivalent to 3 x 10^5 photons per degraded image, or 74 photons per pixel per degraded image over the area of the degraded image. Although it would not be measurable from telescope data, for our computer simulations we also computed the actual mean-squared error of the Fourier modulus estimate:

$$E^2_{|\hat{F}|} = \frac{\sum_{pq}\left(|\hat{F}_{pq}| - |F_{pq}|\right)^2}{\sum_{pq}|F_{pq}|^2} \tag{9}$$

where F_{pq} is assumed to include the weighting factor W_{pq}. A plot of $E_{|\hat{F}|}$, the rms error of the Fourier modulus estimate, versus the number of photons per degraded image is shown in the upper curve of Figure 5.

Since the signal-to-noise ratio of the Fourier modulus estimate tends to decrease with increasing spatial frequencies, one would hope to reconstruct low-frequency (low resolution) features of an object even under very noisy conditions for which the high-frequency information is lost. For this reason, reconstruction experiments were also performed on low resolution versions of the Fourier modulus estimates. Formation of low resolution versions of $|\hat{F}|$ were accomplished by replacing the radius-62 W_{pq} in Eq. (7) by a W_{pq} of the same form, but of radius 16 pixels (i.e., approximately four times coarser resolution than the baseline "high resolution" version). The

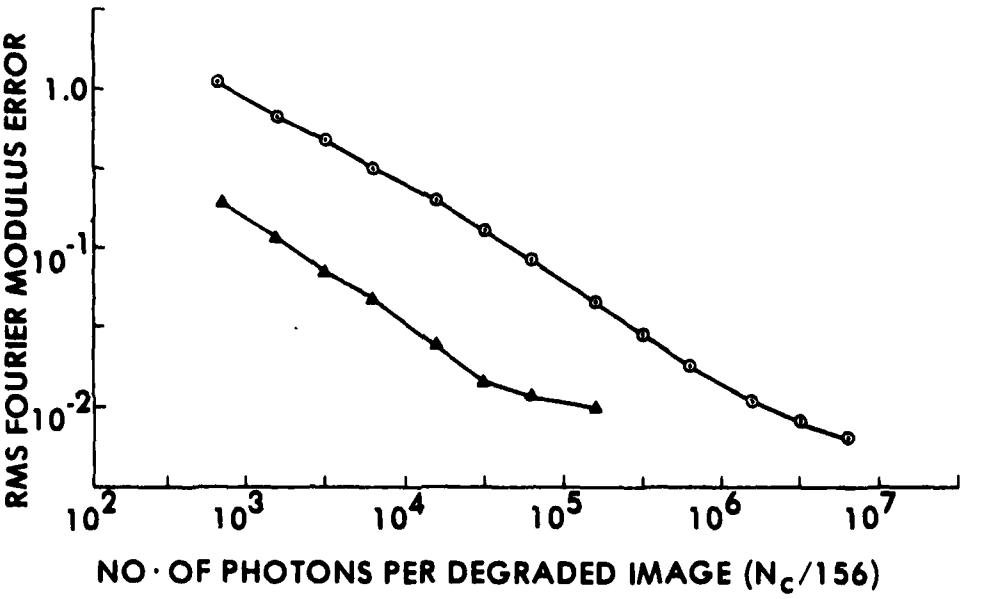

Figure 5. Rms error of Fourier modulus estimate, $E_{|\hat{F}|}$, versus number of photons per degraded image, $N_c/156$. Upper curve: high resolution version; lower curve: low resolution version.

lower curve in Figure 5 shows $E_{|\hat{F}|}$ versus the number of photons per degraded image for the low resolution version of $|\hat{F}|$. The fact that the curve for the low-resolution case is below that of the high-resolution case (that is, the error of the Fourier modulus estimate is lower) confirms the notion that the error increases with increasing spatial frequencies.

3.2 IMAGE CONSTRUCTION RESULTS FROM NOISY FOURIER MODULUS

Image construction by the iterative method (as described in Section 2) was carried out on 13 high-resolution and 8 low-resolution Fourier modulus estimates which were generated in the manner described in Section 3.1. In each case, although useful images were usually available after about 100 iterations, 600 iterations (the same sequence of iterations for all cases) were carried out in order to ensure that the convergence of the algorithm was as complete as was practical.

The rms error E_o, which is a measure of how well the constructed image agrees with the object-domain constraints and Fourier modulus estimate, was reduced to about 0.007 for the lowest-noise case, to 0.05 for the median-noise case, and to 0.4 for the highest-noise case. In no case was E_o driven to zero; that is, in no case did the algorithm converge to a solution that was in perfect agreement both with the Fourier modulus estimate and with the object's nonnegativity constraint. Such agreement would be impossible because the noise present in the Fourier modulus estimate makes that estimate inconsistent with the object's nonnegativity constraint. In particular, if the corresponding estimate of the object's autocorrelation is computed by Fourier transforming $|\hat{F}|^2$, that autocorrelation estimate is found to have regions of negative values. It can easily be shown that an autocorrelation with negative values can arise only from an object with negative values. That is, there can be no nonnegative (physical) object that could give rise to the Fourier modulus estimate $|\hat{F}|$. (In addition, even if the estimate of the object's autocorrelation were nonnegative, then it is still possible that there would be no nonnegative object giving rise to it. Although we do not know in general how to tell if a given function is an autocorrelation function, it can be shown that not all nonnegative symmetric functions are auto-

correlation functions, and a sum of autocorrelation functions is not necessarily an autocorrelation function.) Nevertheless, this iterative image construction method, which relies on the nonnegativity of the solution and strives toward a nonnegative solution, finds a solution that has a minimum amount of negative values; in doing so, it constructs an image that is (at least for cases where only a moderate amount of noise is present) a good approximation to the original object.

The image construction results are shown in Figure 6 and 7 for the high-resolution and low-resolution cases, respectively. Images that came out inverted (rotated in the plane of the page by 180°) were re-inverted in order to take on the same orientation as the reference object. Inverted solutions are always possible since the Fourier modulus of $f(-x)$ equals the Fourier modulus of $f(x)$, for $f(x)$ real valued. Figure 6(E) shows the result for the baseline case. In the high-resolution case, a good quality image, Figure 6(H), was constructed for a photon count (signal-to-noise ratio) ten times worse than the baseline case. A degraded but still recognizable image, Figure 6(K), was constructed for a photon count one hundred times worse than the baseline case. At four hundred times worse photon count than the baseline case, Figure 6(H), it appears that no useful image information remains.

Also shown for comparison in Figures 6(N)-6(U) are short-exposure images with no atmosphere present (diffraction-limited and photon-limited) for the eight lowest signal-to-noise ratio cases, corresponding to Figures 6(F)-6(M), respectively. From this it is seen that a single short-exposure image with no atmosphere present is better than an image constructed from the Fourier modulus estimate based on 156 short-exposure images. One might also wish to compare the image construction results with the sum of 156 photon-limited images with no atmosphere present. For the lowest signal-to-noise ratio case having photoelectron scale factor of 6, the sum of 156 images would be the same as a single image of photelectron scale factor of $936 = 6 \times 156$, which corresponds to a result half way between Figures 6(N) and 6(O).

The low resolution results shown in Figure 7 are for the eight lowest signal-to-noise ratio cases only. Comparing Figure 7 with Figure 6(F)-6(M), for the same number of photon counts, N_c, the constructed images appear to be less noisy in the low-resolution case than in the high-resolution case.

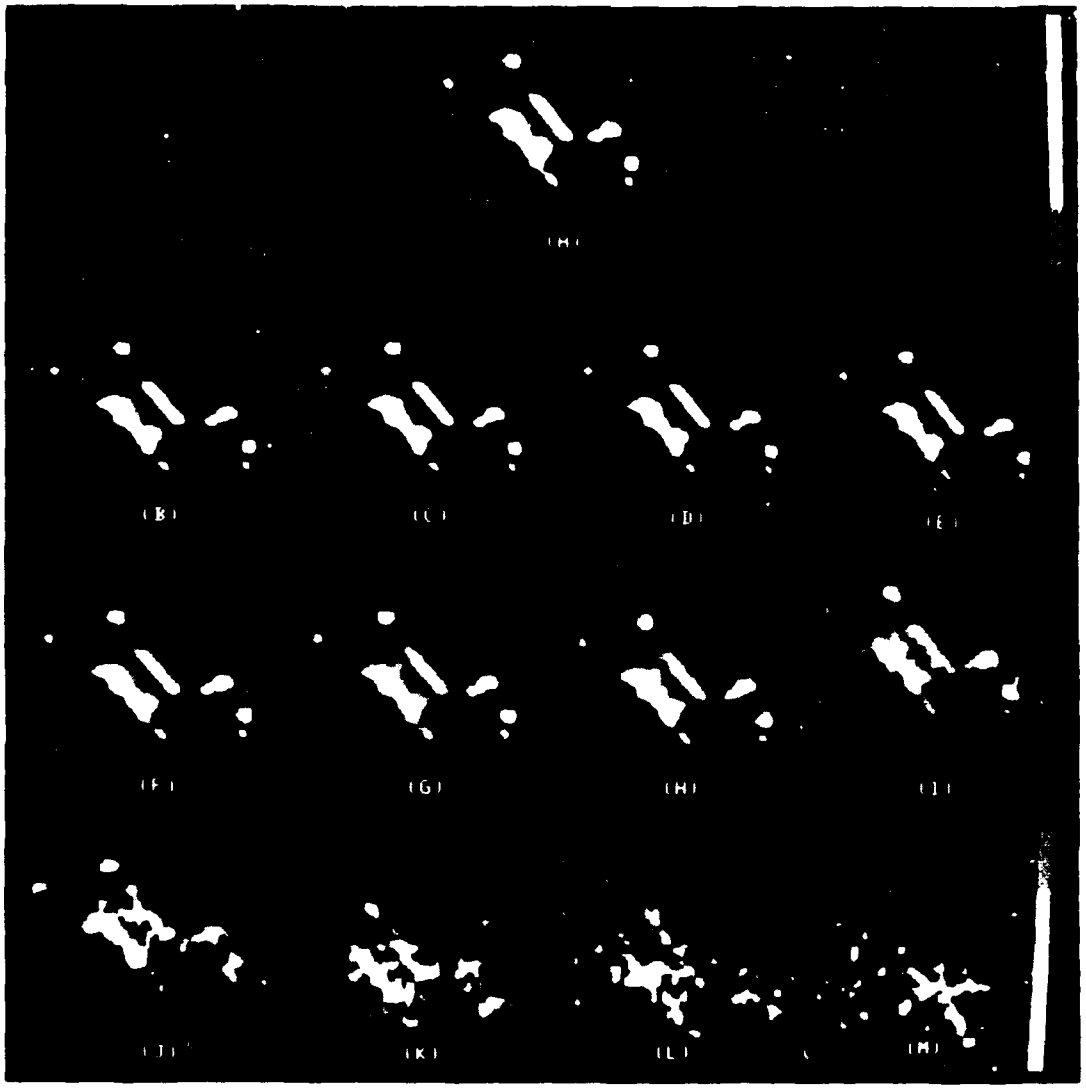

Figure 6. (A) Reference object; (B)-(M) images constructed from Fourier modulus estimates, corresponding to the data points in Figure 5 for the high resolution case, excluding the lowest noise case. The baseline case is (E). Each third image corresponds to a factor of 10 in number of photons detected.

Figure 6. (N)-(U) Photon-limited short-exposure images with no atmosphere present (see text).

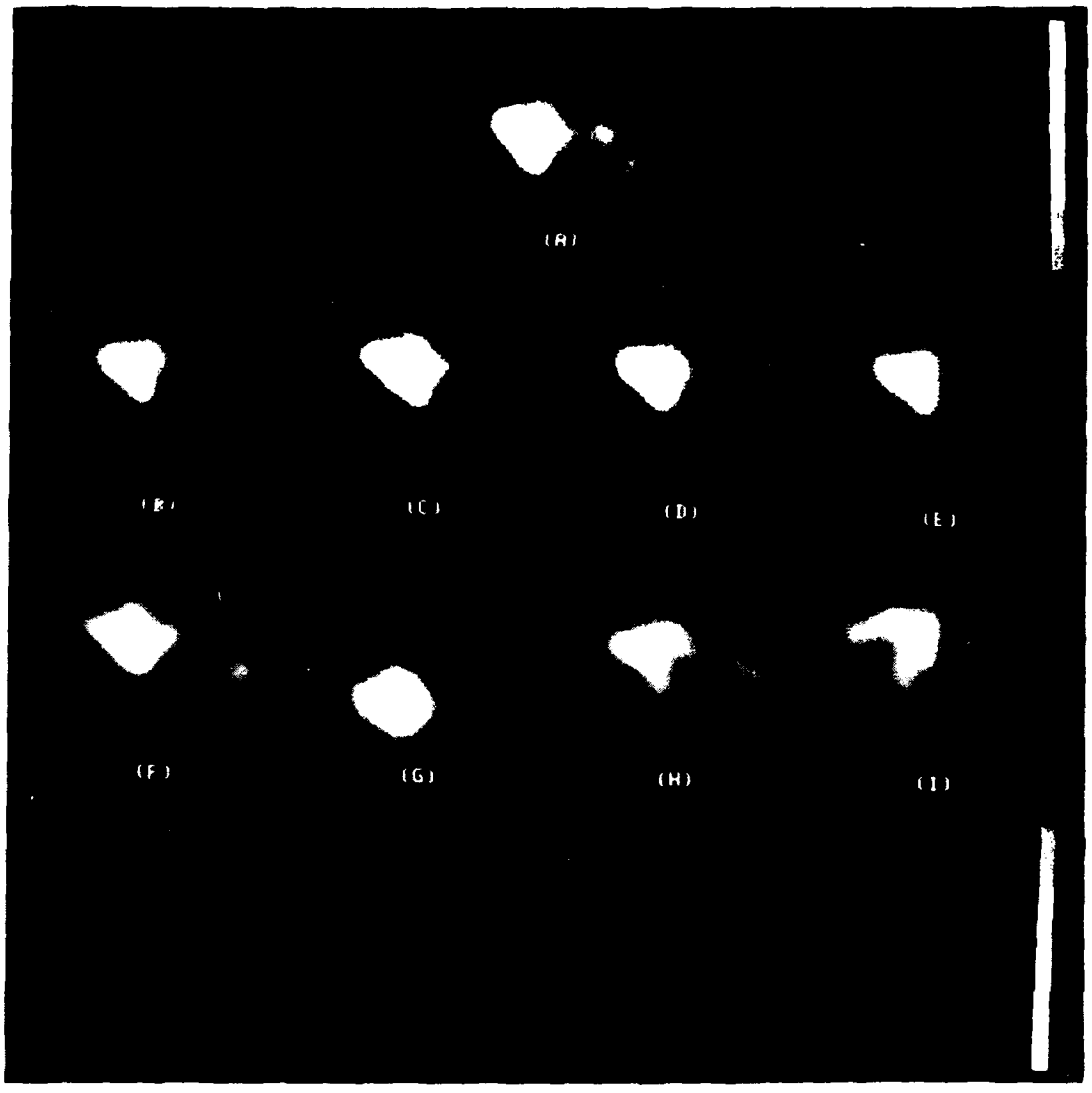

Figure 7. (A) Low resolution version of reference object; (B)-(I) images constructed from low resolution versions of the Fourier modulus estimates, corresponding to the data points in the lower curve of Figure 5.

It should be noted, however, that in the high-resolution case, the noise in the constructed image is mostly in the higher-frequency details, and the lower-frequency components (the coarser details) of the constructed images remain more faithful than the higher-frequency details. Based on just their low frequency content (coarse details), the high-resolution and low-resolution cases appear to be comparable.

Although it would not be measurable from telescope data, for our digital simulations we computed the actual mean-squared error of the constructed image, since we have available the reference object. Before this mean-squared error can be computed, the constructed image must be brought into coincidence with the reference object, since the constructed image may be translated and even spatially inverted relative to the reference object [2]. The choice of whether to invert the image and what translation is required was determined by successively computing the cross-correlations of the reference object with the constructed image at normal and inverted orientations, and searching for the maximum over the two cross-correlations. Inversion of the image (when necessary) was effected by conjugating its Fourier transform, and translation of the image was accomplished by multiplying its Fourier transform by a linear phase factor. The resulting constructed complex Fourier transform $\tilde{G}_{pq}$ was used to compute the mean-squared error

$$\tilde{E}_F^2 = \frac{\sum_{pq} |\tilde{G}_{pq} - F_{pq}|^2}{\sum_{pq} |F_{pq}|^2} \tag{10}$$

which is equivalent to the mean-squared error defined in the image domain as

$$E_o^2 = \frac{\sum_{mn} \left(\tilde{g}_{mn} - f_{mn}\right)^2}{\sum_{mn} f_{mn}^2} = \tilde{E}_F^2 \equiv \tilde{E}^2 \tag{11}$$

where $\tilde{g}_{mn}$ is the translated and possibly inverted version of the constructed image. In Eqs. (10) and (11) the reference object f_{mn} and its Fourier transform are assumed to have been subjected to the same weighting function W_{pq} as the Fourier modulus estimate.

The rms error of the constructed images, $\tilde{E}$, is shown as a function of $E_{|\hat{F}|}$, the rms error of the Fourier modulus estimate, in Figure 8, which shows that $\tilde{E}$ appears to vary approximately as the square root of $E_{|\hat{F}|}$. This approximate square root relationship was not expected — no theoretical results are known that predict this relationship. For a given $E_{|\hat{F}|}$, $\tilde{E}$ is approximately the same for the low resolution cases (triangles) as for the high resolution cases (circles). Therefore, except for possible savings in computation time there does not seem to be any advantage to low-pass filtering the data before applying the iterative algorithm. A more sophisticated filter such as Wiener filter could, on the other hand, prove advantageous.

For the low noise cases E did not go below 0.1 although the square root of $E_{|\hat{F}|}$ was well below that level. The cause of this error in the low noise cases seems to have resulted not from the noise but from the stagnation of the algorithm at an image that perhaps is at a local minimum of error, but not at a global minimum. These images look like the reference object with a low contrast sinusoidal pattern superimposed (or as stripes across the image). Figures 9(a)-9(d) show four different images constructed from the same Fourier modulus estimate ($N_c = 9.5 \times 10^8$), each arrived at by the same sequence of iterations but with different arrays of random numbers as the initial input to the first iteration. The stripes appear in each image, but with different orientations and spatial frequencies. This phenomenon was noticed earlier [2], but a complete explanation of it has not been available. Further discussion of this phenomenon is given in Section 5. Also shown in Figure 9 are four different images constructed from the same Fourier modulus for a higher noise case ($N_c = 9.5 \times 10^6$). In this case the stripes do not occur; but a noticeable amount of random noise occurs in the background of the images, and the details of that noise are different for each constructed image.

The image construction results shown in Figure 6 were arrived at from initial inputs consisting of random numbers. In addition, images were also constructed using the reference object as the initial input. Although such an initial input is unrealistic from the point of view that in the real world the reference object would not be known, those image construction results were interesting because they shed some light on the problem of the stripes.

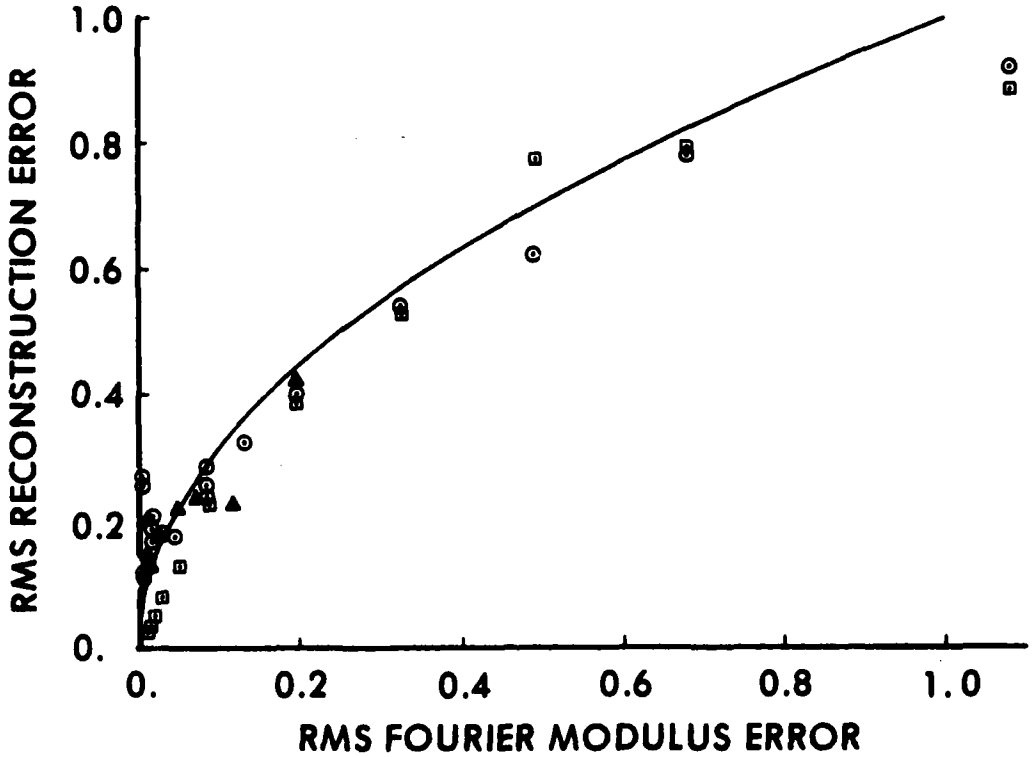

Figure 8. Rms error of constructed images, $\tilde{E}$, versus rms error of the Fourier modulus estimates, $E_{|\hat{F}|}$. Circles indicate high resolution versions and triangles indicate low resolution versions. Squares indicate results when the reference object was used as the initial input to the algorithm (see text). The solid line shows $\sqrt{E_{|\hat{F}|}}$ for comparison.

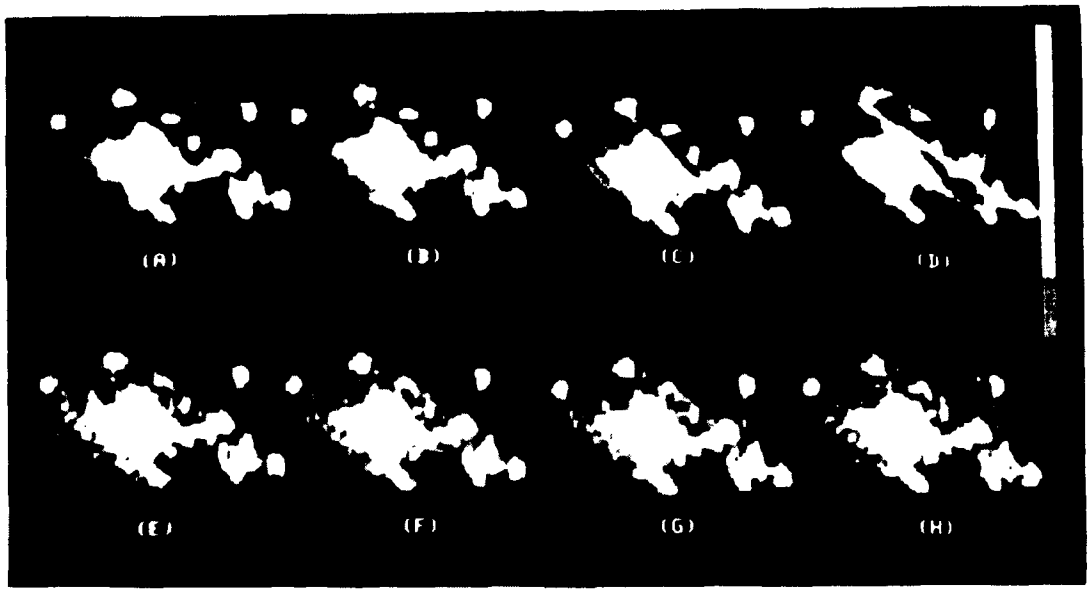

Figure 9. Four images constructed using different starting inputs. (A)-(D) Low noise case (6.1×10^6 photons per degraded image) showing stripes; (E)-(H) higher noise case (6.1×10^4 per photons per degraded image). These pictures were intentionally overexposed in order to emphasize the stripes and the background noise.

When starting with the reference object as the initial input, we have something that is not in perfect agreement with the noisy Fourier modulus estimate. As the iterations progress, the output image departs from the reference object while becoming in better agreement with the Fourier modulus estimate. Finally, the iterations stagnate at a point where the result is in as good agreement as possible with the simultaneous constraints of object nonnegativity and Fourier modulus equalling the Fourier modulus estimate.

For the medium to high noise cases, the constructed images resulting from the reference object as the initial input were comparable to the constructed images resulting from random numbers as the initial input; in addition, the error measures E_0 and $\tilde{E}$ were comparable for the two cases. For the low noise cases, the constructed images resulting from the reference object as the initial input were comparable in appearance to the constructed images resulting from random numbers as the initial input except that no stripes were present. In addition, both the error measures E_0 and $\tilde{E}$ were considerably less than the values for the case of the random initial input. $\tilde{E}$ for this case is plotted in Figure 8 along with the case of the random initial input, where it is seen that $\tilde{E}$ approaches zero as $E_{|\hat{F}|}$ approaches zero, as one would expect. For the four lowest noise cases, the error E_0 for the case of the random initial input versus the case of the reference object as initial input was 0.00737 vs 0.00333, 0.00748 vs 0.00391, 0.00794 vs 0.00526, and 0.0114 vs 0.00933. For higher amounts of noise E_0 was comparable in the two cases. Therefore, for the low noise cases one can distinguish the local minimum having stripes from the global minimum not having stripes by the value of the rms error E_0. It is this fact that a smaller error E_0 occurred for the constructed image not having stripes that leads us to believe that the stripes represent a problem of encountering a local minimum and do not represent a fundamental uniqueness problem.

The most important result from this set of experiments on the noise properties is that as the noise increases, the quality of the constructed images degrades in a gradual and predictable manner. Furthermore, the quality of the constructed images is very good for the realistic signal-to-noise ratios expected for imaging satellites. Images of this quality were obtained in spite of the fact that Wiener filtering was not performed. By adding a post

processing step of Wiener filtering the images, improved image quality may be expected.

4
UNIQUENESS OF IMAGES CONSTRUCTED FROM FOURIER MODULUS

It is well known that for the one-dimensional case the Fourier modulus is usually ambiguous [11]. That is, there may be many objects that have the same Fourier modulus. Going further, there may even be many real, nonnegative objects that have the same Fourier modulus. One therefore might question why one should even attempt to construct an image from Fourier modulus data if one could get many different solutions. Fortunately the one-dimensional analysis does not carry over into two dimensions, and, as will be shown later, the solution almost always is unique for the two-dimensional case. In Section 4.1 the previously known theory is briefly reviewed and new experimental construction results are shown in Section 4.2 for a variety of objects.

4.1 UNIQUENESS THEORY

We first consider the one-dimensional case, although the problem in which we are most interested is two-dimensional. Switching to continuous variables, the Fourier transform relationship, of which Eq. (1) is a discrete form, is

$$F(u) = \int_{-\infty}^{\infty} f(x) e^{-i2\pi ux}\, dx \tag{12}$$

If $f(x)$ is of finite extent, that is, if it is zero outside a finite interval $[a, b]$, then the function $F(z)$ is an entire function (analytic everywhere) of exponential type. The variable z is a complex variable of which u is the real part. Such functions are completely specified by their complex zeroes z_i, $i = 1, 2, \ldots$, satisfying $F(z_i) = 0$. In particular, from the Hadamard factorization theorem we have [12]

$$F(z) = Az^q \prod_{i=1}^{\infty} (1 - z/z_i) \tag{13}$$

where A is a constant and q is the order of the zero at $z = 0$.

The reason that the one-dimensional case is usually not unique is as follows. In theory, since $F(z)$ is analytic, given any finite segment of $F(z)$, $F(z)$ can be determined everywhere by analytic continuation. Similarly, since $F(z)$ is analytic, so is $F(z)\overline{F}(\overline{z})$, which is equal to $|F(u)|^2$ on the real line. (The overbar indicates complex conjugation.) Therefore, given $|F(u)|^2$ it is theoretically possible to determine the complex zeroes of $F(z)\overline{F}(\overline{z})$. If the complex zeroes of $F(z)$ were known, then Eq. (13) could be used to determine $F(z)$ and in particular $F(u)$. However, for each zero z_i of $F(z)$, $F(z)\overline{F}(\overline{z}) = 0$ both at z_i and at $\overline{z}_i$. Therefore for each non-real-valued complex zero of $F(z)$ there is a two-fold ambiguity of the solution. If there are m complex zeroes then there would be 2^{m-1} different solutions, and in general m is infinite. In general it is not known, however, what number of solutions are nonnegative.

Although the uniqueness problem is very severe in the one-dimensional case, it fortunately does not appear to be a problem in the two-dimensional case. Bruck and Sodin [13] analyzed the case of an object made up of an array of delta-functions. The Fourier transform then reduces to a discrete sum, and the discrete sum can be shown to be equivalent to a polynomial of complex variables. The zeroes (roots) of the polynomial are associated with the complex zeroes discussed above. It can then be shown that the ambiguity of the solution is determined by the number of factors into which the polynomial can be factored. In the one-dimensional case a polynomial can always be expressed as the product of m prime factors, where m is equal to the order of the polynomial, which is equal to the number of discrete points across the object. Therefore, for the one-dimensional case there are 2^{m-1} solutions. On the other hand, two-dimensional polynomials are rarely factorable. Therefore, for the two-dimensional case the solution is usually unique (to within a 180° rotation and a translation).

It can be argued that this analysis can be extended to the case of a continuous, extended object (as opposed to a sampled object) by noting that $F(z)$ for a continuous object can be closely approximated by a polynomial [14]. Therefore, although further analytical work is required to definitively answer the question of uniqueness for continuous objects in two-dimensions,

one would expect the solution to be generally unique (except for very special cases) in two dimensions.

Fried [15] has considered the special case for which the Fourier transform is separable in its two orthogonal coordinates, that is, it can be written as the product of two one-dimensional functions (and if the Fourier transform is separable, then so is the object function). This case can be shown to have a high degree of non-uniqueness. The high degree of ambiguity is expected since the separability condition changes the two-dimensional problem into two one-dimensional problems, and the high degree of ambiguity is well known in one dimension, as discussed earlier.

Fried [15] goes one step further and shows how to generate an arbitrary number of nonnegative (one-dimensional or separable two-dimensional) functions having the same Fourier modulus. He has since found that the functions generated by his method tend to be smooth

4.2 UNIQUENESS EXPERIMENTS

The uniqueness of the solution was empirically tested on several different objects in order to provide a practical answer to the uniqueness question.

Digitized photographs of several different satellites were provided to ERIM by B.L. McGlamery (Visibility Laboratory, U.C. San Diego). Since it was suspected that the uniqueness property may depend on the complexity of the object, we computed several versions of each satellite, each version at a different resolution (at a different magnification). The lower resolution versions provided examples of less complicated objects.

The method of generating lower resolution versions was to resample the fine resolution images on a coarser grid. Points on the coarser grid that fell between the points on the finer grid were given values according to a two-dimensional separable triangular filter operating on the four nearest neighbor points on the finer grid. This type of resampling does <u>not</u> give an

[illegible] demagnification [illegible] it has a tendency to overemphasize some features of the object and miss others. However, for the purpose of these experiments an accurate demagnification was not required; it was only desired that a smaller, less complicated object be synthesized.

The objects used are listed in Table 1. In order to avoid the possibility of aliasing, the objects were initially all scaled to fit within a square of size 64 by 64 pixels, which was imbedded in an array of size 128 by 128. The magnification factors required for the initial scaling are listed in Table 1. If a telescope of diameter 1.6 meters and a wavelength of 550 nm were used, and the image sample size were equivalent to $(\lambda/2D)$ = 550 nm/3.2 m = 1.719×10^{-7} radians = 0.03545 are-sec per pixel, then the apparent distances corresponding to the objects of size 64 pixels are given by (image scale in meters per pixel) $(2D/\lambda)$, which are listed in the last column of Table 1. In addition to objects of size 64 pixels, objects of size 32, 16, 8 and 4 pixels were generated using the resampling method described above. That is, a total of 40 test objects (8 objects at 5 magnifications each) were used in the experiments. The smaller, lower-resolution objects can be thought of as being at *proportionally greater* distances from the telescope. Because of the way that the resampling was done, the objects "of size 4 pixels" are in fact only 3 pixels across; in addition, except for the Film No. 508 and 608 cases, one pixel dominates the others; consequently, the objects of size 4 pixels tend to look very much like single point scatterers.

The Fourier modulus data for each test object was generated by Fourier transforming the test object, then multiplying the complex Fourier transform by W, the weighting function due to a circular telescope aperture, and then taking the modulus (or magnitude). The weighting function is given by the autocorrelation of a circular aperture of diameter 62 pixels in the Fourier domain. For this set of experiments the effects of diffraction due to the telescope aperture were included, but the Fourier modulus data was otherwise free of error. For comparison with the construction results, the inverse Fourier transform of the weighted complex Fourier transform was computed. The resulting image, which is referred to as the reference object, is equivalent to a diffraction-limited image of the object.

The same set of 340 iterations as discussed in Section 2 was us[illegible] each of the forty test cases. Figures 10 to 17 show the reference obje[illegible] and a corresponding constructed image for all forty cases. Images that came out inverted were re-inverted in order to take on the same orientation as the reference object.

A problem that occurred was that the algorithm usually did not converge completely to a solution: it usually stagnated at a local minimum at which it produced an image of good quality but with a set of stripes superimposed across the image. When the algorithm stagnated at such a local minimum, it was not possible to determine with certainty whether the solution it was converging toward was exactly the same as the reference object. As discussed in Section 3, the stagnation at an output image having stripes is most likely a problem of algorithm stagnation at a local minimum of E_0 and does not represent a uniqueness problem. In almost all of the different constructed images shown in Figures 10-17, the primary difference between the constructed image and the reference object is the presence of the stripes. Therefore we conclude from those cases that if the algorithm were improved in such a way as to avoid stagnation with stripes, then it would probably converge to an output image identical to the reference object. That is, these results imply that for most cases the solution is unique.

The stripes are usually more difficult to see when reproduced than they are when the image is viewed on a T.V. monitor, which has greater dynamic range than a paper print of the image. Usually there is a single set of stripes across the image. In any given image the stripes have an average period and angular orientation, but across the image the stripes vary significantly about those averages. In some cases, more than one set of stripes appear in a given image; for example, in Figure 12(B) there are strong (high contrast) stripes both horizontally and at about a 45 degree angle. The stripes extend over the entire field-of-view but have maximum contrast over the extent of the object. The fact that the stripes extend beyond the known extent of the object (which is half the diameter of the autocorrelation) will probably enable us, some time in the future, to develop an algorithm to detect them and eliminate them.

[illegible] lists the rms error E_0, as defined by Eq. (5), for the forty constructed images. This is a measure of how well the constructed image agrees with the simultaneous constraints of nonnegativity and having a Fourier modulus equal to the Fourier modulus of the reference object; that is, it is a measure of how close it is to a solution. For a given size of object, constructed images with larger values of E_0 are known to be farther from a solution. Therefore, for example, the 32-pixel size and 16-pixel size constructed images of Film No. 302 shown in Figures 12(D) and (F) should probably be ignored because they are much farther from solutions than are the constructed images for the other objects (and so they are not necessarily an indication of non-uniqueness).

If the cases that did not converge very close to a solution (having large values of E_0) are ignored, and if perturbations due to stripes are ignored, then most, but not all, of the image construction results shown in Figures 10-17 seem to indicate that the solutions are unique. The most disturbing departure from uniqueness came in the case of the 64-pixel size of Film No. 401, FLTSATCOM. The constructed image has the same overall shape as the reference object but differs from it in its details, despite the fact that for this object an additional 380 iterations were performed. Subsequent runs of the algorithm using different starting inputs encountered similar problems for this object. From Figure 14(A) one can see that for this particular object its bright central part is nearly circularly symmetric. Since a circularly symmetric object can be described as a function of a single variable, its radial coordinate, one could hypothesize that such objects would have the same high degree of ambiguity as one-dimensional objects, but this is not known. Therefore, although most objects of interest are probably unique, there appear to be special classes of objects for which the solution is not unique. From the results shown in Figures 10-17 it appears that the non-unique (ambiguous) cases are the exceptions rather than the rule.

TABLE 1
OBJECTS FOR UNIQUENESS STUDY

Film No.	Object Description	Unscaled Pixel Size	Magnification for 64-Pixel Width	Apparent Distance for 64-Pixel Width (km)
204	P72-2 Sensor Testbed (A)	0.0174m	0.267	379
205	P72-2 Sensor Testbed (B)	0.0174m	0.267	379
302	777 Communications Sat(A)	0.0174m	0.267	379
314	777 Communications Sat(B)	0.0174m	0.279	363
401	FLTSATCOM	0.0581m	0.250	1352
509	LST (A)	0.0871m	0.356	1423
508	LST (B)	0.0871m	0.291	1741
608	SURVSATCOM	0.116m	0.356	1896

TABLE 2
RMS ERROR E_0 OF CONSTRUCTION RESULTS FOR
UNIQUENESS STUDY

Object (Film No.)	Object Size (Pixels) 64	32	16	8	4
204	0.0327	0.0234	0.00914	0.00051	0.00048
205	0.0262	0.00421	0.00074	0.00058	0.00049
302	0.0189	0.0553	0.0154	0.00071	0.00053
314	0.0156	0.00268	0.00813	0.00164	0.00055
401	0.00240	0.00101	0.00061	0.00050	0.00048
509	0.00782	0.00660	0.00072	0.00053	0.00048
508	0.00296	0.00179	0.00197	0.00071	0.00048
608	0.00368	0.00169	0.00073	0.00100	0.00054

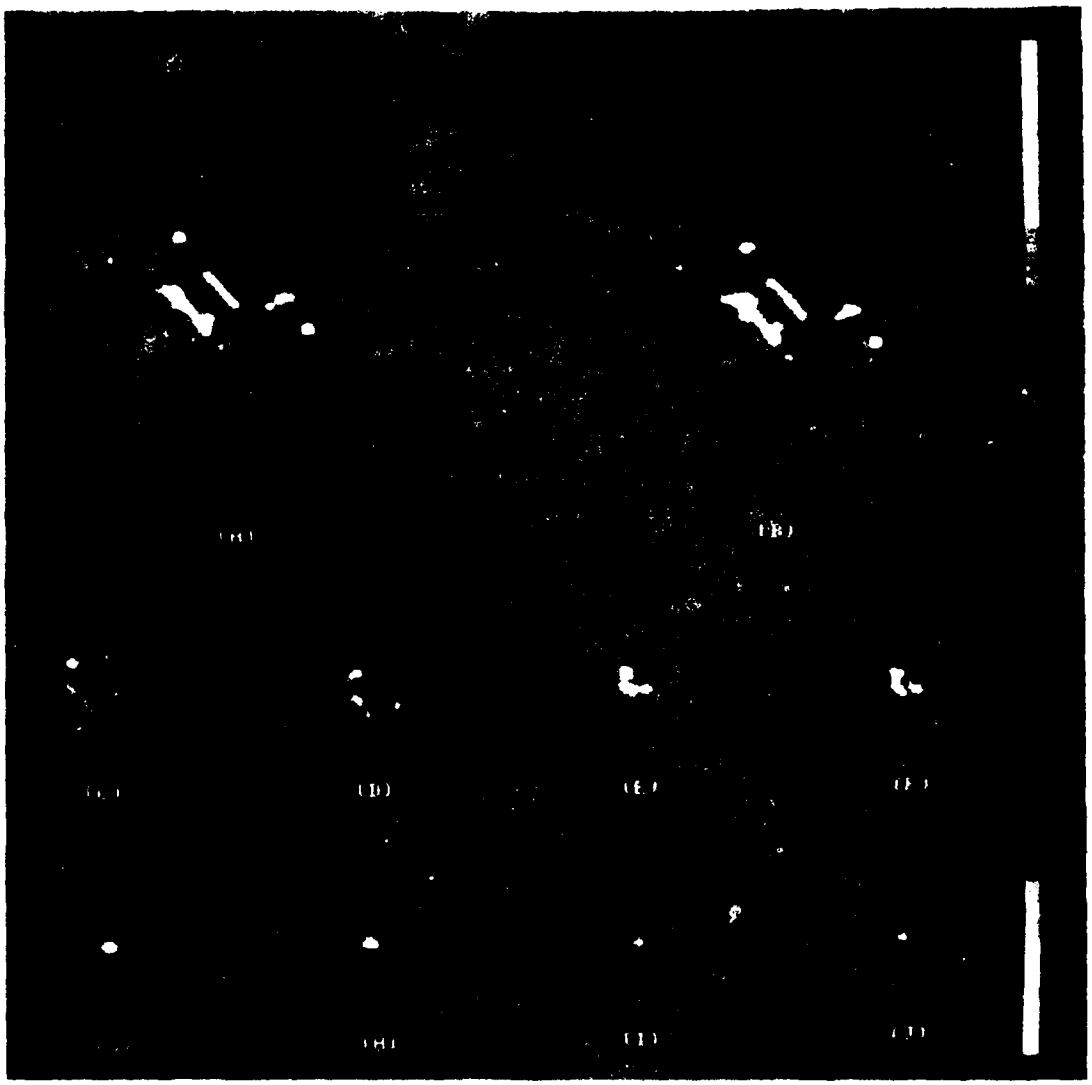

Figure 10. Reference objects and constructed images for Film No. 204, P72-2(A). Reference object and constructed image for (A, B) 64-pixel width, (C, D) 32-pixel width, (E, F) 16-pixel width, (G, H) 8-pixel width, and (I, J) 4-pixel width.

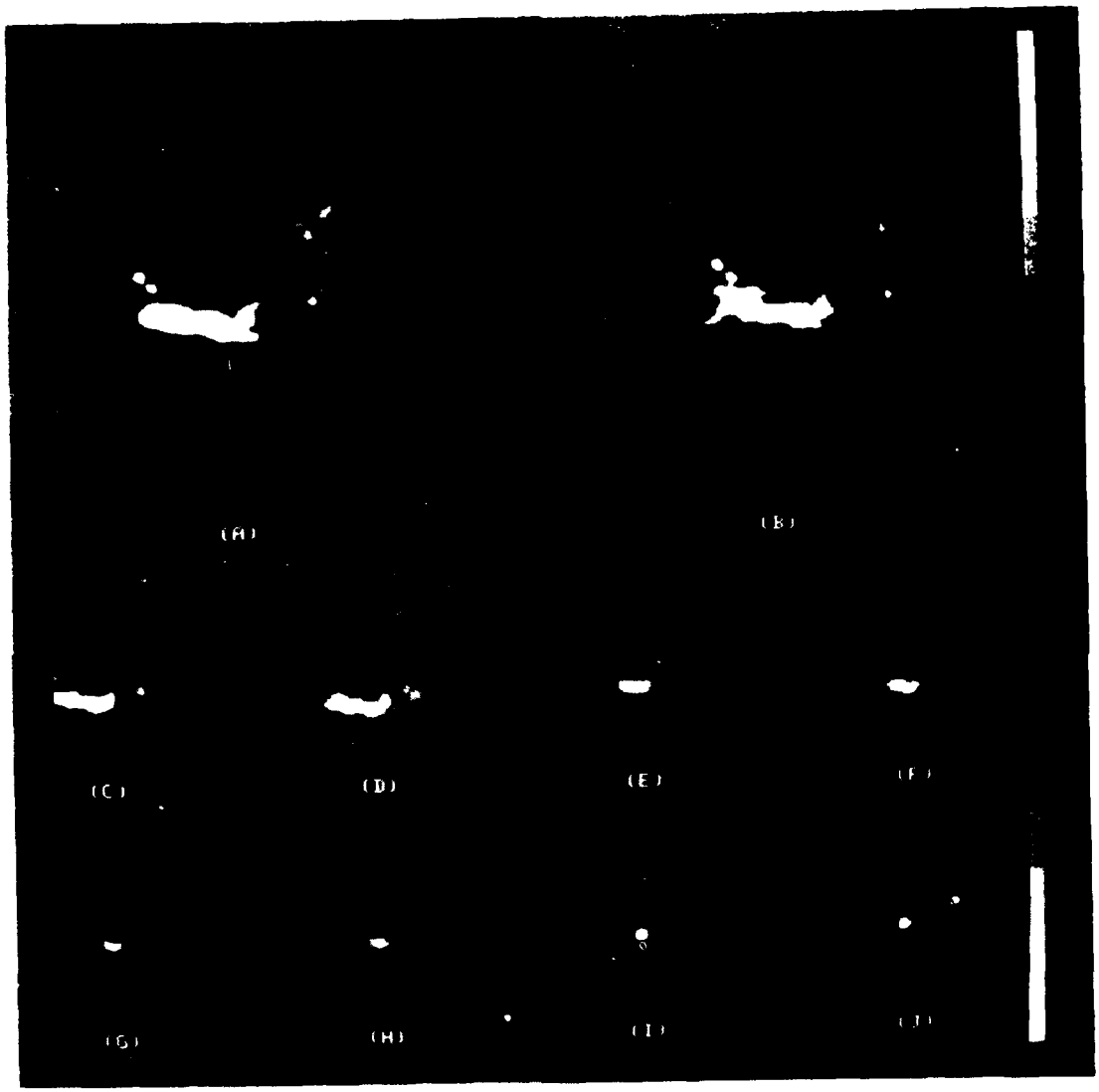

Figure 11. Reference objects and constructed images for Film No. 205, P72-2(B). Reference object and constructed image for (A, B) 64-pixel width, (C, D) 32-pixel width, (E, F) 16-pixel width, (G, H) 8-pixel width, and (I, J) 4-pixel width.

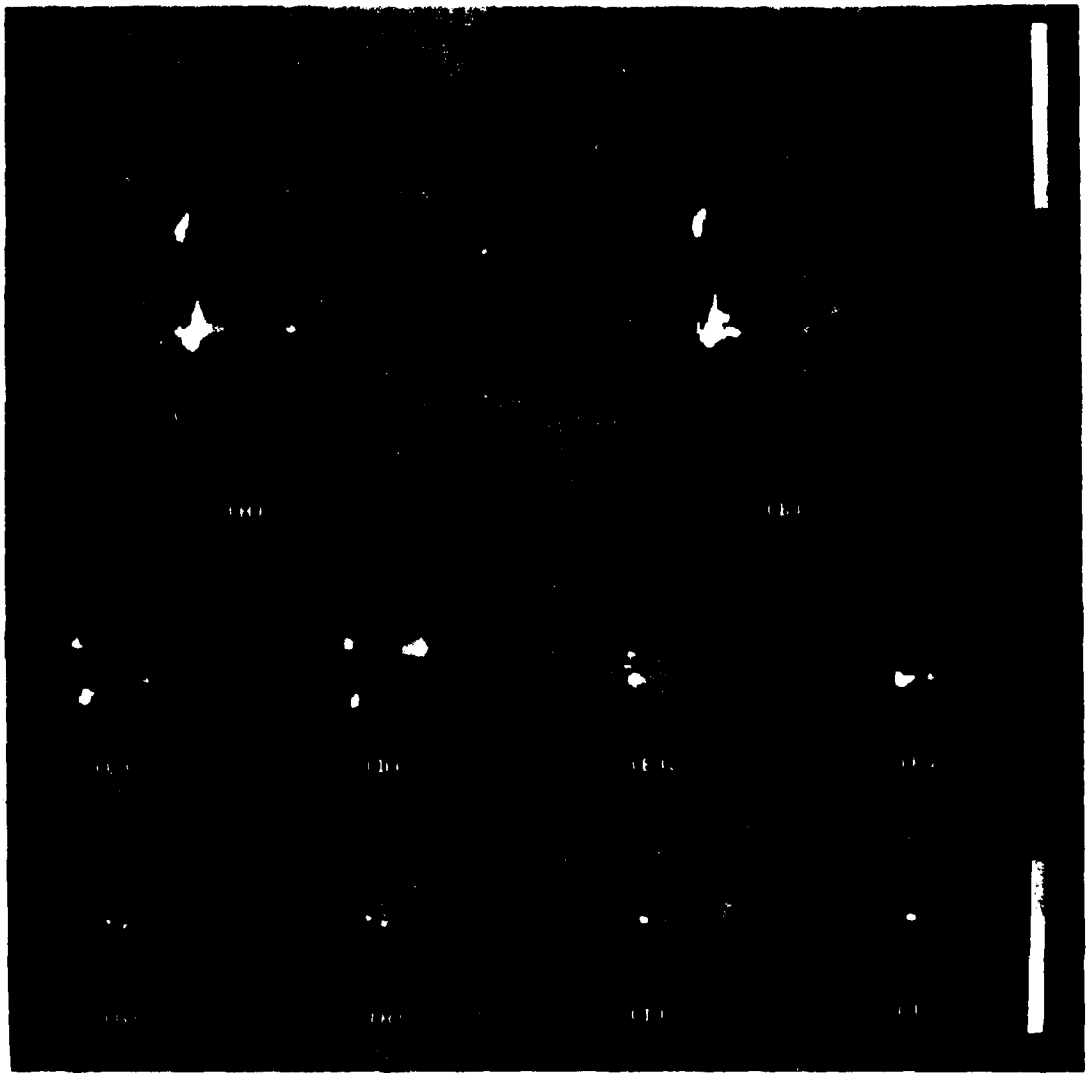

Figure 12. Reference objects and constructed images for Film No. 302, 777(A). Reference object and constructed image for (A, B) 64-pixel width, (C, D) 32-pixel width, (E, F) 16-pixel width, (G, H) 8-pixel width, and (I, J) 4-pixel width.

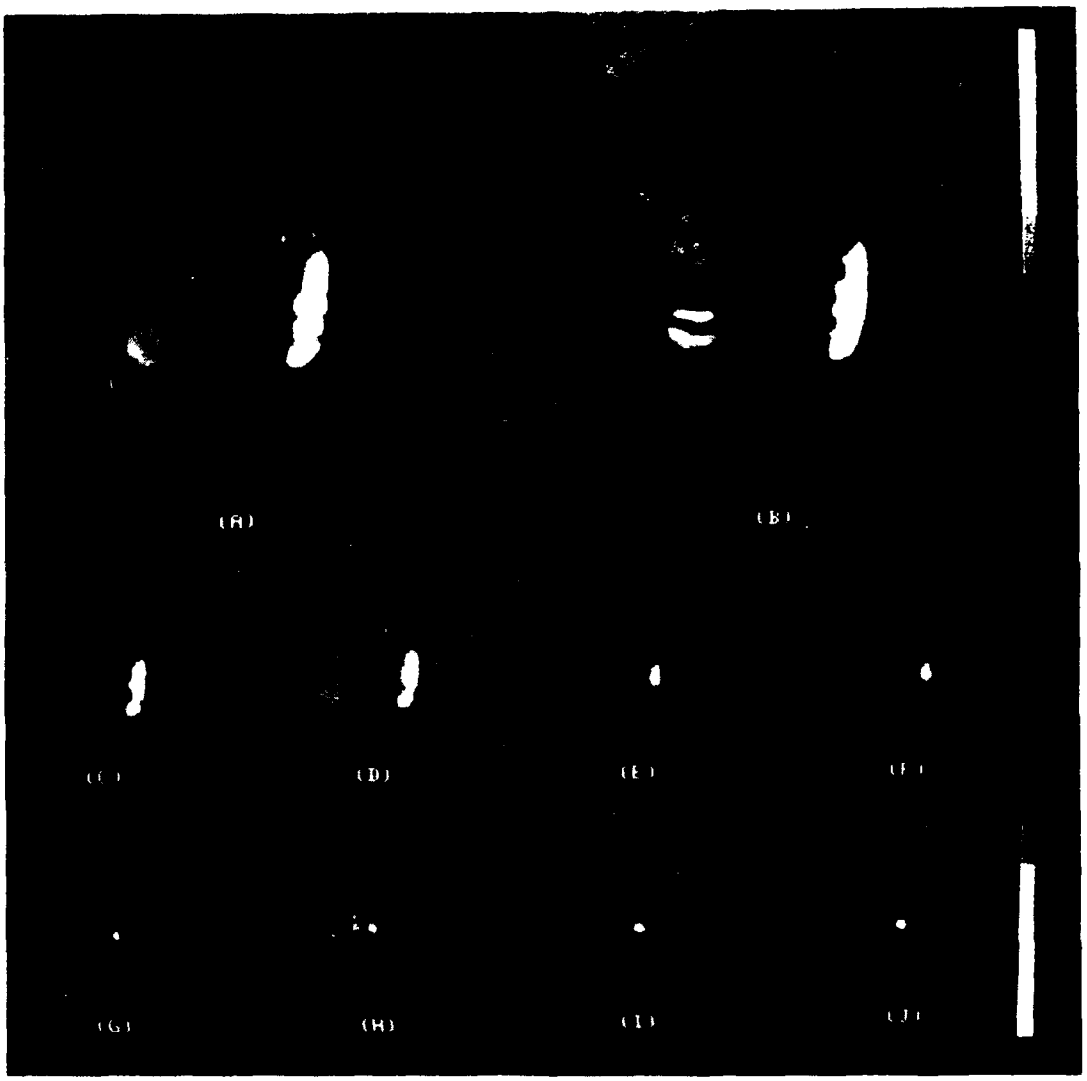

Figure 13. Reference objects and constructed images for Film No. 314, 777(B). Reference object and constructed image for (A, B) 64-pixel width, (C, D) 32-pixel width, (E, F) 16-pixel width, (G, H) 8-pixel width, and (I, J) 4-pixel width.

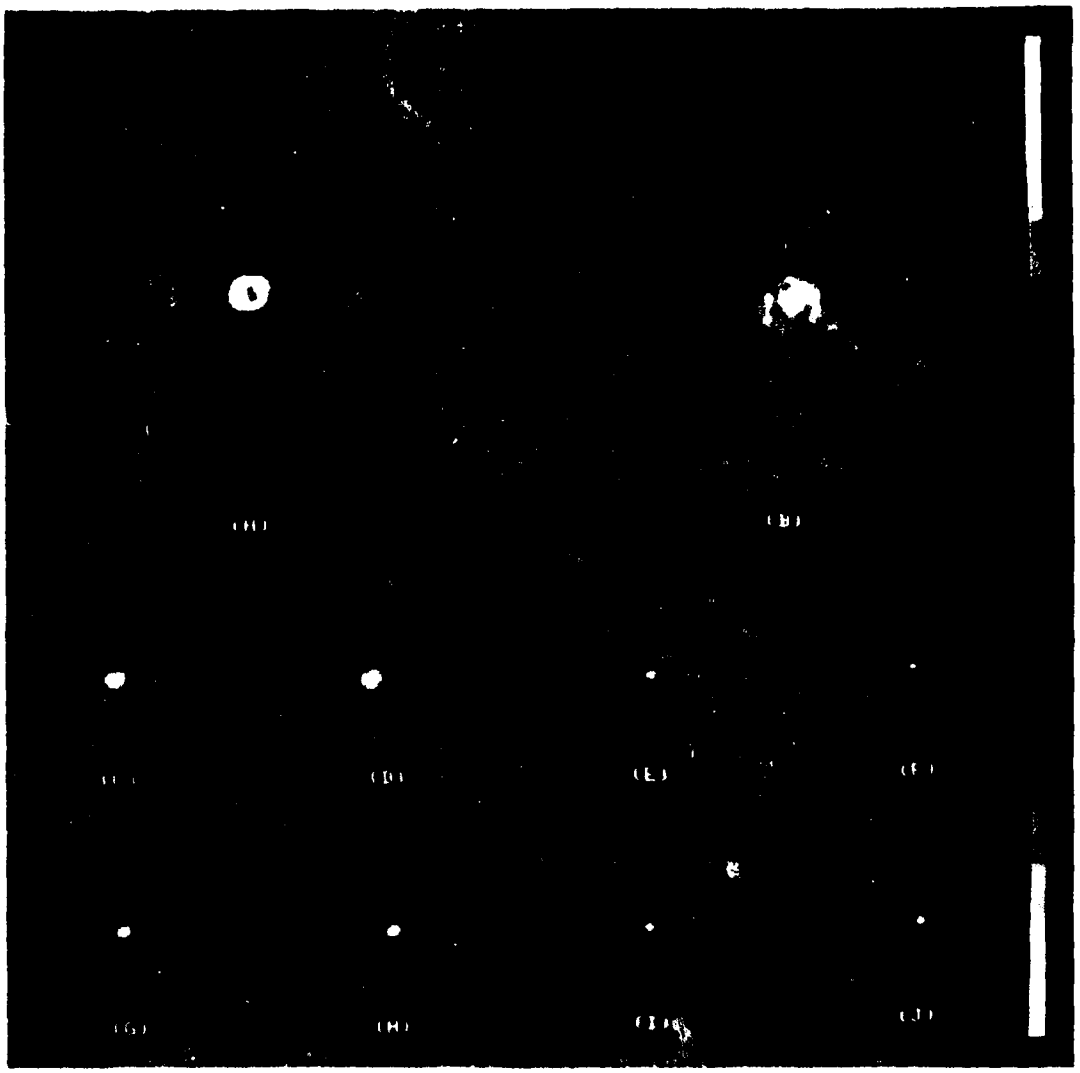

Figure 14. Reference objects and constructed images for Film No. 401, FLTSATCOM. Reference object and constructed image for (A, B) 64-pixel width, (C, D) 32-pixel width, (E, F) 16-pixel width, (G, H) 8-pixel width, and (I, J) 4-pixel width.

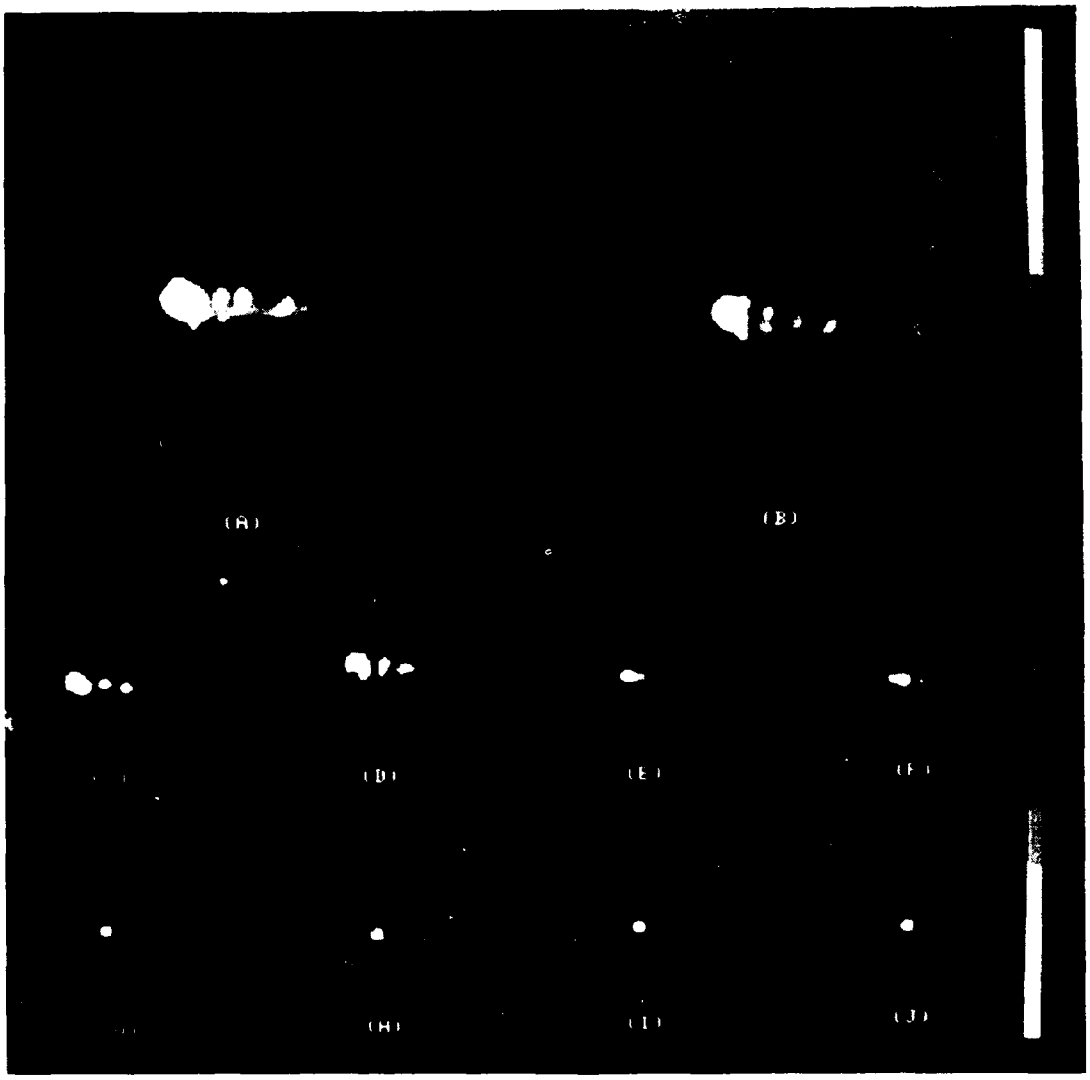

Figure 15. Reference objects and constructed images for Film No. 509, LST(A). Reference object and constructed image for (A, B) 64-pixel width, (C, D) 32-pixel width, (E, F) 16-pixel width, (G, H) 8-pixel width, and (I, J) 4-pixel width.

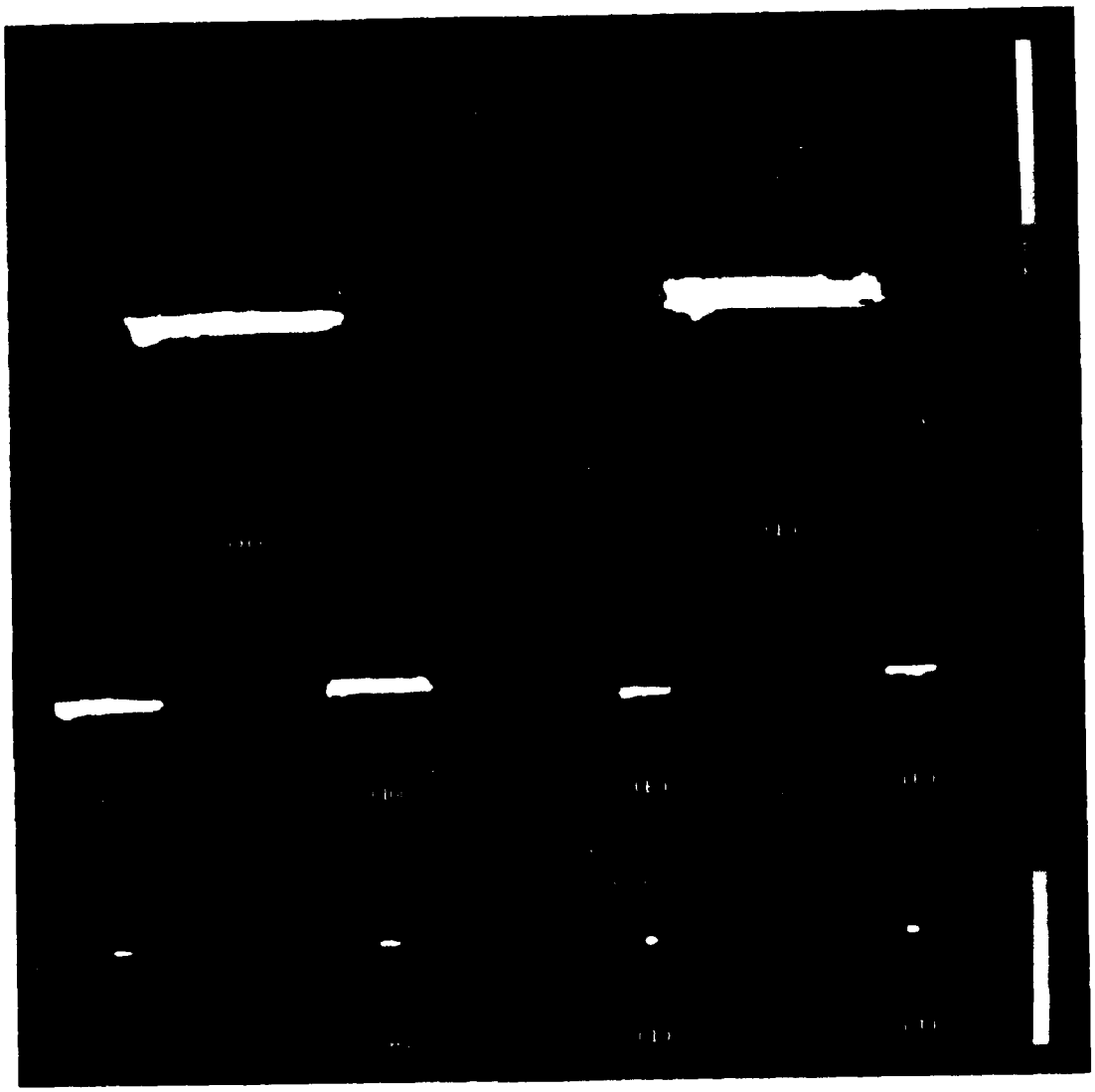

Figure 16. Reference objects and constructed images for Film No. 508, LST(B). Reference object and constructed image for (A, B) 64-pixel width, (C, D) 32-pixel width, (E, F) 16-pixel width, (G, H) 8-pixel width, and (I, J) 4-pixel width.

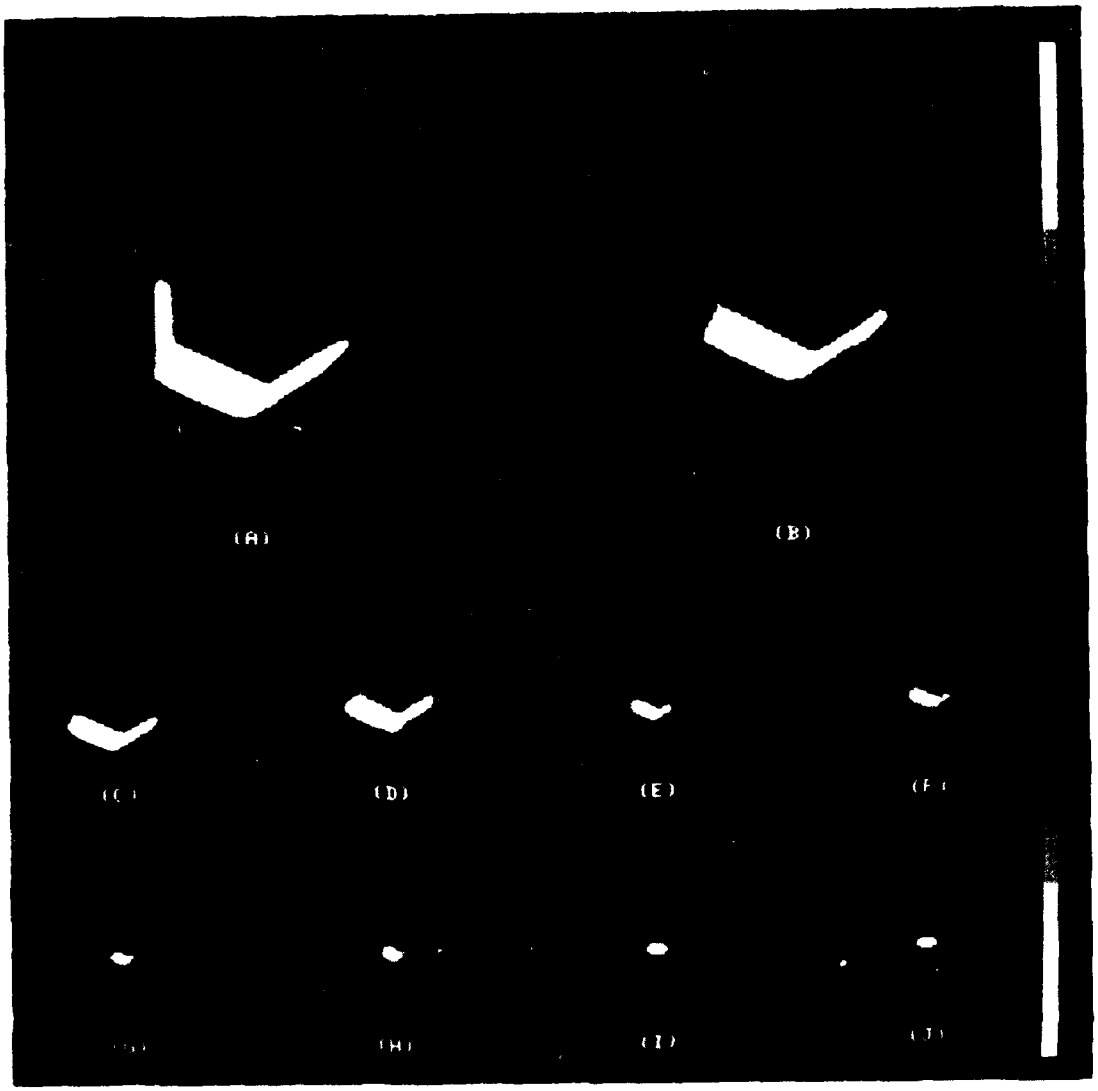

Figure 17. Reference objects and constructed images for Film No. 608, SURVSATCOM. Reference object and constructed image for (A, B) 64-pixel width, (C, D) 32-pixel width, (E, F) 16-pixel width, (G, H) 8-pixel width, and (I, J) 4-pixel width.

5
ALGORITHM CONVERGENCE

Several different aspects of the convergence of the algorithm are of interest. A few variations of the algorithm were compared for convergence speed. Investigations were made into the convergence speed as a function of object complexity and of Fourier modulus signal-to-noise ratio. Attempts were made to cause the solution to move away from a local minimum characterized by the stripes discussed in Sections 3 and 4.

5.1 COMPARISON OF DIFFERENT ALGORITHMS

Four different versions of the algorithm were compared. All four versions use the same first three steps described in Section 2. They differ in the method in which the new input g_{K+1} is chosen. The first method, which we call the <u>error-reduction approach</u>, is given by Eq. (2) in Section 2:

$$g_{k+1,mn} = \begin{cases} g'_{k,mn}, & (m, n) \notin \gamma \\ 0, & (m, n) \in \gamma \end{cases} \tag{14}$$

where $g_{k,mn}$ and $g'_{k,mn}$ are the input and output, respectively, at the kth iteration and γ is the set of points at which $g'_{k,mn}$ violates the object-domain constraints. The principal object-domain constraint is that g' be nonnegative everywhere; an auxiliary constraint is that the extent (diameter) of the object not exceed the known diameter which is half the diameter of the given autocorrelation. For the error-reduction approach the new input is equal to the current output modified to satisfy the object-domain constraints. Satisfying the object domain constraints consists of setting the output to zero wherever it violates the constraints. In Appendix A is a proof that the error reduction approach converges in the sense that the mean squared error, as defined in Eqs. (4) and (5) in Section 2, is monotonically decreasing with each successive iteration.

In addition to the error-reduction approach, three different versions of the more general input-output approach were investigated. The basic idea

behind the input-output approach is that the first three operations of the algorithm — Fourier transformation, satisfaction of Fourier-domain constraints, and inverse Fourier transformation -- can be viewed as a nonlinear system having an input g and an output g'. By appropriate changes in the input one attempts to drive the output to satisfy the object-domain constraints. Since the output by definition satisfies the Fourier-domain constraints, it is a solution to our problem if it can be made to satisfy the object-domain constraints.

For a problem very similar to the one at hand, it has been shown that for small changes in the input, the expected value of the corresponding change in the output is a constant, α, times the change in the input [4]. Since additional nonlinear terms also appear in the output, the change in the output due to a particular change in the input cannot be predicted exactly. Nevertheless, by appropriate changes in the input, the output can be pushed in the general direction that is desired. If a change Δg_{mn} is desired in the output, then a logical choice for a change in the input to achieve that change in the output would be $\beta \Delta g_{mn}$, where β is a constant ideally equal to α^{-1}. For the problem at hand, the desired change in the output is

$$\Delta g_{mn} = \begin{cases} 0, & (m, n) \notin \gamma \\ -g'_{mn}, & (m, n) \in \gamma \end{cases} \tag{15}$$

that is, where the constraints are satisfied one does not require a change of the output, but where the constraints are violated, the desired change in the output is one that drives it to a value of zero (and therefore the desired change is the negative of the output at those points). Therefore a logical choice for the next input is $g + \beta \Delta g$, that is,

$$g_{k+1,mn} = \begin{cases} g_{k,mn}, & (m,n) \notin \gamma \\ g_{k,mn} - \beta g'_{k,mn}, & (m,n) \in \gamma \end{cases} \tag{16}$$

We will refer to the use of Eq. (16) as the <u>basic input-output</u> approach.

An interesting property of the nonlinear system (consisting of the three steps mentioned above) is that if an output g' is used as an input, then its output will be itself. Since the Fourier transform of g' already satisfies the Fourier-domain constraints, g' is unaffected as it goes through the system. Therefore, irrespective of what input actually resulted in the output g', the output g' can be considered to have resulted from itself as an input. From this point of view, another logical choice of the next input is

$$g_{k+1,mn} = \begin{cases} g'_{k,mn}, & (m,n) \notin \gamma \\ g'_{k,mn} - \beta g'_{k,mn}, & (m,n) \in \gamma \end{cases} \tag{17}$$

We will refer to the use of Eq. (17) as the <u>output-output</u> approach.

Note that if $\beta = 1$ in Eq. (17), then the output-output approach reduces to the error-reduction approach of Eq. (14). Since the optimum value of β is usually not unity, the error-reduction approach can be looked on as a suboptimal version of a more general approach.

A fourth method of choosing the next input which we investigated is a combination of the upper line of Eq. (17) with the lower line of Eq. (16):

$$g_{k+1,mn} = \begin{cases} g'_{k,mn}, & (m,n) \notin \gamma \\ g_{k,mn} - \beta g'_{k,mn}, & (m,n) \in \gamma \end{cases} \tag{18}$$

We will refer to the use of Eq. (18) as the <u>hybrid input-output</u> approach. The hybrid input-output approach is an attempt to avoid a stagnation problem that tends to occur with the output-output approach. The output-output approach often works itself into a situation in which the output on successive iterations does not change, despite being far from a solution. For the hybrid input-output approach, on the other hand, if at a given pixel (m, n) the output remains negative for more than one iteration, then the corresponding point in the input continues to grow larger and larger until eventually that output point must go nonnegative.

The four approaches discussed above were compared by using them on the same Fourier modulus data and with the same starting input. For each approach several different values of the parameter β were tried. The principal problem with the error-reduction approach is that it tends to stagnate after a few iterations. The starting point for the iterations was chosen to be a partially constructed image of the Film No. 509, LST(A) object (at a 64-pixel size), on which the error-reduction approach was making very slow progress. Ten iterations of each of the four approaches followed by ten iterations of the error-reduction approach (that is, a total of twenty iterations) were performed using that same starting input. The reason that each approach was followed by ten iterations of the errorreduction approach is that in some cases definite progress is being made with an input-output approach even though the rms error gets worse with each iteration. The relationship between the rms error and the visual image quality is not fully understood, although of course one would expect a high degree of correlation between the two. For the approaches for which the rms error does not seem to be a good indication of the image quality, we found that the rms error could be made to be a good measure of the image quality by performing a few (say ten) iterations of the error-reduction approach on the results of the input-output approach.

Figure 18 shows a plot of the rms error after the twenty iterations for each of the input-output approaches as a function of the parameter β. Recall that the output-output approach with $\beta = 1.0$ is equivalent to the error reduction approach. Figure 18 shows that the hybrid input-output approach is superior to the others in this case, and that the optimal value of β is about unity.

The manner in which the diameter constraint (limiting the diameter of the constructed image to half the diameter of the autocorrelation) was imposed was found to have a significant impact on the convergence speed. At the beginning of this program the strategy for applying the diameter constraint was to impose it very loosely (i.e., allow the image to have a larger diameter) for the early iterations, then tighten up the diameter for later iterations after the image distribution became better confined to an area of the desired size. This strategy helped to avoid the previously encountered

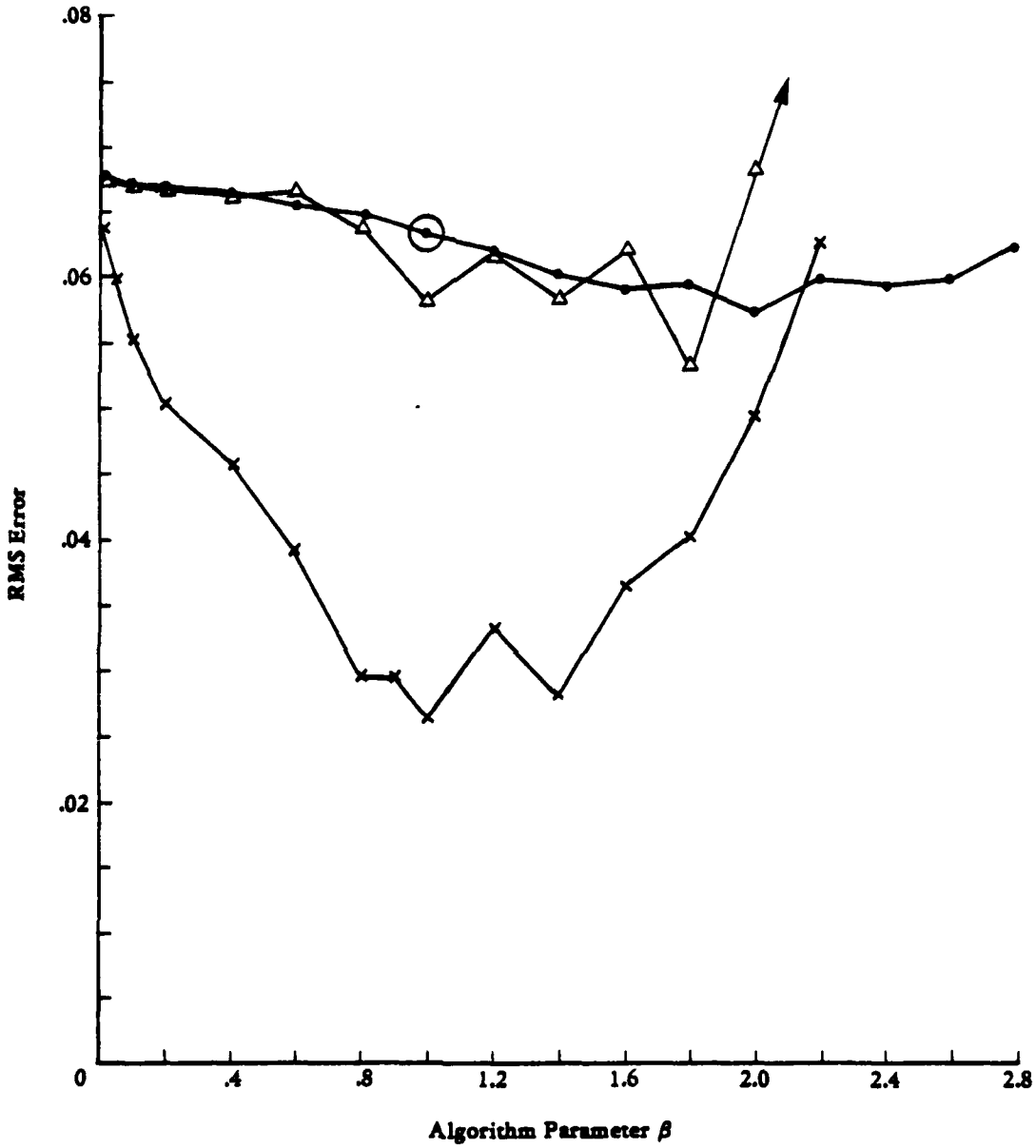

Figure 18. Rms error, E_0, after sequence of 20 iterations versus algorithm parameter β for the basic input-output approach (Δ), the output-output approach (•) and the hybrid input-output approach (x).

problem of having the diameter constraint inadvertently chopping off an edge of the desired image. It was discovered that reversing the sequence resulted in an increase in convergence speed: apply a very tight diameter constraint for the early iterations, and loosen that constraint as the iterations progress. This strategy helps to move energy from the regions clearly outside the object's support to within the objects support during the early iterations. This results in a convergence speed-up by as much as a factor of two.

5.2 DATA DEPENDENCY OF CONVERGENCE

The convergence speed of the algorithm depends both on the complexity of the object and upon the signal-to-noise ratio of the Fourier modulus data. The most convenient scale by which convergence is measured is the rms error E_0 or E_F, both of which are consistently meaningful only after a few iterations of the error reduction approach are performed.

The data generated during the studies of the noise properties of the constructed images show that the number of iterations required was the least for the data of the lowest signal-to-noise ratio. For the data having the very worst signal-to-noise ratio (photoelectron scale factor = 6), only a few iterations were required for convergence. That is to say, after just a few iterations no further progress could be made although E_0 was still large, and the solution had gone as far as it usefully could. For the higher signal-to-noise ratio cases, additional iterations further reduced the rms error, so in that sense the convergence time was longer.

The data generated during the studies of the uniqueness of the solution showed that the objects of lesser complexity (smaller magnification) converged to lower values of rms error E_0 after fewer iterations than the more complex objects. However, the total number of iterations performed before the algorithm stagnated showed only a weak dependency on object complexity. For the cases of low object complexity stagnation occurred at considerably lower values of E_0 than for cases of higher object complexity, but stagnation tended to occur sooner for cases of low object complexity.

5.3 THE STRIPES PHENOMENON

As mentioned in Sections 3 and 4 the algorithm often stagnates at a local minimum characterized by a pattern of stripes across the image. In most cases the stripes are barely noticeable and are of low contrast superimposed on an otherwise excellent constructed image. In some cases the stripes are of high enough contrast to be objectionable, although they still permit the object to be recognized. As shown in Section 3, different starting inputs converge to images having stripes of different angular orientations and spatial frequencies (periods). There seems to be a tendency for the stripes to be oriented at the same angle as a prominent feature of the object. The stripes extend over the entire field-of-view, beyond the known diameter of the object. The contrast of the stripes tends to be greater over the extent of the object and less outside the extent of the object. The stripes appear only when the signal-to-noise ratio is high.

We believe that the existence of the stripes does not represent a fundamental uniqueness problem. When the algorithm stagnates on an output having stripes, the rms errors E_0 and E_F are never zero, and so it is known that it is not exactly a solution, although it is usually close to a solution. If the algorithm happens to find the solution free of stripes, then the rms error E_0 is lower than for the case having stripes, providing a way to distinguish the correct solution from the solution having stripes. In addition, since a valid solution cannot have a diameter exceeding half the diameter of the autocorrelation, the fact that the stripes extend beyond that diameter provides a way to distinguish the correct solution from a solution having stripes.

For the one-dimensional case it is known that if a single pair of complex zeroes is moved (to locations other than their conjugates) around symmetrically in the Fourier complex plane, then the result in the image plane can be a function similar to the original but having a sinusoid added over the interval of its support [12]. This particular operation results in a Fourier transform with a Fourier modulus different from the original Fourier modulus; therefore the new object created does not cause a problem of uniqueness. Furthermore, this one-dimensional analysis does not carry over directly into

two dimensions. Nevertheless, this one-dimensional phenomenon might ultimately be connected in some way with the stripes phenomenon.

An attempt was made at moving away from the constructed image having stripes. After the algorithm converged to an image having stripes and seemed to stagnate there, random noise was added to the image and then further iterations were performed. It was found that the algorithm quickly converged back to an image with essentially the same stripes, even when large amounts of noise had been added. Only by starting with a different initial input having no stripes present could one converge to an image having a different set of stripes. Further work will be necessary to develop a method of breaking away from stagnation at local minima having stripes.

6
CONCLUSIONS AND RECOMMENDATIONS FOR FUTURE RESEARCH

The results shown here indicate that construction of images by the iterative method from Fourier modulus data provided by stellar speckle interferometry should prove to be successful for imaging earth-orbiting satellites. With the levels of photon noise present in practical situations it should be possible to construct images that are diffraction-limited in resolution. The solution can generally be counted on to be unambiguous (i.e., unique) except for special classes of objects, for example, objects that can be described as separable functions. The image construction algorithm has been developed to a point were convergence requires about 100 iterations, which takes less than two minutes on an array processor (Floating Point System AP-120B) for array sizes 128 by 128.

More particularly, the major results of this research effort are as follows. The rms error of the constructed images increases in a gradual and predictable manner as the rms error of the Fourier modulus estimate increases, roughly as the square root of the rms error of the Fourier modulus estimate. For photon noise levels up to ten times worse than the baseline case, the quality of the constructed image is good. The most recent theory of the uniqueness of the solution suggests, and our experimental results appear to confirm, that the solution is usually unique for two-dimensional objects, both for objects of high complexity (large space-bandwidth product) and low complexity. These results were obscured, however, by an inability to converge completely to a solution in many cases. The algorithm has a tendency to stagnate at a local minimum characterized by a set of stripes across an otherwise recognizable image of the object. As the signal-to-noise ratio of the Fourier modulus data decreases, the ambiguity of the solution increases, but that ambiguity takes the form of noise in the constructed image rather than a complete change in the basic characteristics of the image. Fewer iterations of the algorithm were needed in the low signal-to-noise ratio cases, but the images were correspondingly poorer. Images of greater complexity tended to take a larger number of iterations than images of lower complexity. The convergence speed of the algorithm was increased by the manner in which the diameter constraint was imposed. A comparative study of

a few different versions of the algorithm showed that, among the approaches tried, the hybrid input-output approach converges the fastest by a wide margin.

The most critical questions have been answered successfully by this research, but important aspects of the problem remain to be studied.

Although useful images are obtained in spite of it, the stripes phenomenon remains as a puzzling hindrance to the complete convergence of the algorithm to a solution. Theoretical analysis is needed to understand why the stripes occur and how they might be dealt with. Further effort should be expended to determine ways of automatically identifying the presence of the stripes and having the algorithm reject them. Once this problem is solved, the uniqueness experiments should be repeated in order to determine with greater certainty whether the solution is usually unique.

A potential source of error not addressed in this research project is the estimation of the MTF of the speckle interferometry process. Computer simulations should be performed in order to determine the effect of errors in the MTF estimate on the constructed image and whether they affect the uniqueness of the solution. In addition, there may be situations for which it is not always convenient or practical to obtain an estimate of the speckle MTF from a reference star. Therefore, alternative methods of estimating the speckle MTF should be studied and compared, including model fitting, the Worden subtract method, and the clipping method [10].

Further development of the algorithm itself is needed to make it converge in real time. More variations of the algorithm should be compared over a wider range of circumstances. In addition, major modifications of the algorithm may be called for. A particularly promising line of attack would be to apply the discipline of control theory to the input-output system concept.

Image construction experiments should be carried out on actual telescope data gathered on orbiting satellites to demonstrate its usefulness in solving the space object identification problem and to discover what additional problems need to be overcome when handling data from a real sensor.

Comparison of the image construction results from noisy Fourier modulus data should be made both with (computer simulated) images constructed by the

Knox-Thompson method [16] and with images from a compensated imaging system. As the reflectivity of the object decreases, there is some point beyond which it is no longer possible to accurately sense the wavefront deformation, and the compensated imaging system would no longer adequately correct for atmospheric turbulence. However, under the same severely photon-limited case, speckle interferometry can continue to function since it integrates over many frames and can ultimately have a higher signal-to-noise ratio than the compensated imaging system which must correct for turbulence based on measurements made over an interval of time of only a few milliseconds. Computer simulations should be carried out on the Knox-Thompson method using the same simulated data that was generated for the noise properties study described in this report. Then using existing computer-simulated results for the Fourier modulus image construction method and for compensated imaging, a comparison of the three methods should be made for various levels of photon noise. It may also be desirable to vary the turbulence parameter r_0. To make the comparison complete, the same type of Wiener filtering should be performed on the Knox-Thompson and Fourier modulus image construction results as is done on the images from the compensated imaging system.

Methods of combining the image construction from speckle interferometry Fourier modulus data with compensated imaging systems should be explored. It may be possible to have a compensated imaging system utilize the iterative method for those instances where low light levels hinder the ability to track the wavefront deformation caused by the turbulent atmosphere. Experiments both with simulated compensated images and eventually with real data from a compensated imaging system would be needed. Most simply, the iterative method can be thought of as another post-processing step to obtain improved imagery from the compensated imaging system. When compensated images from the system being developed at AMOS on Maui become available, if they are not diffraction-limited they should be additionally post-processed using the iterative algorithm.

For the case of tumbling or rotating objects, methods will have to be developed to take these effects into consideration. For general time-varying objects it may be possible to "lock on" to the image: after acquiring an image at a given time, as the object changes and new data is collected, only a

few iterations of the algorithm may be required to converge on the new image if information about the previous image is utilized.

Methods of increasing the signal-to-noise ratio of the data to ensure good quality constructed images should be developed. One method of increasing the signal-to-noise ratio is to extend the spectral bandwidth of speckle interferometry. A present limitation on the spectral bandwidth is the wavelength dependence of the impulse response for a given optical path difference caused by the atmosphere. It may be possible to create a wavelength-independent impulse response using an optical system composed of wavelength-sensitive optics, such as holographic optical elements.

Finally, the iterative method could be applied to a number of other problems of interest to the Air Force. It can be applied to any reconstruction problem for which only partial information is available about an object, wavefront, or signal and only partial information is available about its Fourier transform. Such applications include, in addition to Fourier modulus image construction, wavefront sensing, spectral extrapolation, and X-ray crystallography phase retrieval. The iterative method can also be applied to synthesis problems for which one wants both a function and its Fourier transform to satisfy a given set of constraints or have certain desirable properties. Such applications include spectrum shaping and the design of lens pupil functions, antenna array phases, radar signals, and digital filters.

APPENDIX A
CONVERGENCE PROOF

In this appendix it is shown that for the error-reduction approach the error monotonically decreases at each iteration.

The kth iteration begins with $g_{k,mn}$, an estimate of the object that satisfies the object-domain constraints. First $g_{k,mn}$ is Fourier transformed, resulting in $G_{k,pq} = |G_{k,pq}| \exp(i\phi_{k,pq})$. Then in the Fourier domain, $G_{k,pq}$ is replaced by $G'_{k,pq} = |F_{pq}| \exp(i\phi_{k,pq})$. The unnormalized mean-squared error is defined in the Fourier domain as

$$E_{Fk}^2 = \frac{1}{N^2} \sum_{pq} (|G_{k,pq}| - |F_{pq}|)^2 \tag{A1}$$

where $p,q = 0, 1, \ldots, N-1$, which can be expressed as

$$E_{Fk}^2 = \frac{1}{N^2} \sum_{pq} |N_{k,pq}|^2 \tag{A2}$$

where

$$N_{k,pq} = G'_{k,pq} - G_{k,pq} = (|F_{pq}| - |G_{k,pq}|) \exp(i\phi_{k,pq}) \tag{A3}$$

Forming the new Fourier transform $G'_{k,pq}$ and inverse Fourier transforming results in

$$g'_{k,mn} = \mathcal{F}^{-1}[G'_{k,pq}] = g_{k,mn} + n_{k,mn} \tag{A4}$$

where $n_{k,mn} = \mathcal{F}^{-1}[N_{k,pq}]$.

The new estimate of the object is formed by setting $g'_{k,mn}$ equal to zero wherever it violates the constraints:

$$g_{k+1,mn} = \begin{cases} g'_{k,mn}, & (m,n) \notin \gamma \\ 0, & (m,n) \in \gamma \end{cases} \tag{A5}$$

Let $g_{k+1,mn}$ be expressed in terms of $g_{k,mn}$ as follows

$$g_{k+1,mn} = g'_{k,mn} + d_{k,mn} = g_{k,mn} + n_{k,mn} + d_{k,mn} \tag{A6}$$

where

$$d_{k,mn} = g_{k+1,mn} - g'_{k,mn} = g_{k+1,mn} - g_{k,mn} - n_{k,mn} \tag{A7}$$

The unnormalized mean squared error in the object domain is defined as

$$E^2_{Ok} = \sum_{mn\varepsilon\gamma} (g'_{k,mn})^2 = \sum_{mn} (d_{k,mn})^2 \tag{A8}$$

And by applying Parseval's theorem, Eq. (A2) becomes

$$E^2_{Fk} = \sum_{mn} (n_{k,mn})^2 \tag{A9}$$

In the following we will show that $|d_{k,mn}| \leq |n_{k,mn}|$ for all (m,n), proving that $E^2_{Ok} \leq E^2_{Fk}$. (1) For (m,n) where $g'_{k,mn}$ satisfies the constraints [i.e., (m,n) γ], $d_{k,mn} = 0$, and so $|d_{k,mn}| \leq |n_{k,mn}|$. (2) For (m,n) where $g'_{k,mn}$ is negative, $g_{k+1,mn} = 0$ and, from Eq. (A7)

$$d_{k,mn} = - g'_{k,mn} = -g_{k,mn} - n_{k,mn}$$

Since $g'_{k,mn}$ is negative, $d_{k,mn}$ is *nonnegative*. Furthermore, since $g_{k,mn}$ is nonnegative we have

$$d_{k,mn} \leq d_{k,mn} + g_{k,mn} = - n_{k,mn}$$

and so $|d_{k,mn}| \leq |n_{k,mn}|$. (3) For (m,n) where the object is known to be zero (for the case in which the object's diameter is known and that constraint is imposed), $g_{k+1,mn} = g_{k,mn} = 0$, also leaving $d_{k,mn} = - n_{k,mn}$; and so $|d_{k,mn}| \leq |n_{k,mn}|$. Therefore, since $|d_{k,mn}| \leq |n_{k,mn}|$ for all (m,n), then from Eqs. (A8) and (A9) we have

$$E^2_{Ok} \leq E^2_{Fk} \tag{A10}$$

Fourier transforming Eq. (A7),

$$D_{k,pq} = G_{k+1,pq} - G'_{k,pq} \tag{A11}$$

and so

$$|D_{k,pq}|^2 = |G_{k+1,pq}|^2 + |G'_{k,pq}|^2 - 2\,\mathrm{Re}[G'_{k,pq}\,\bar{G}_{k+1,pq}] \tag{A12}$$

where an overbar denotes complex conjugation and Re the real part. From Eq. (A3),

$$N_{k+1,pq} = G'_{k+1,pq} - G_{k+1,pq} \tag{A13}$$

and so

$$|N_{k+1,pq}|^2 = |G'_{k+1,pq}|^2 + |G_{k+1,pq}|^2 - 2\,\mathrm{Re}[G'_{k+1,pq}\,\bar{G}_{k+1,pq}] \tag{A14}$$

Taking the difference between Eq. (A12) and Eq. (A14) and using the fact that $|G'_{k,pq}| = |G'_{k+1,pq}| = |F_{pq}|$, we have

$$|D_{k,pq}|^2 - |N_{k+1,pq}|^2 = 2\,\mathrm{Re}[G'_{k+1,pq}\,\bar{G}_{k+1,pq}] - 2\,\mathrm{Re}[G'_{k,pq}\,\bar{G}_{k+1,pq}]$$

$$= 2\,|F_{pq}|\cdot|G_{k+1,pq}|\,[1 - \cos\theta_{pq}] \geq 0 \tag{A15}$$

where $\theta(u) = \arg[G'_{k,pq}\,\bar{G}_{k+1,pq}]$. And therefore for all (p,q),

$$|N_{k+1,pq}| \leq |D_{k,pq}| \tag{A16}$$

This result can also be easily seen from the geometry of Figure A1. The result is the same irrespective of whether $|G_{k+1,pq}|$ is greater than or less than $|F_{pq}|$. Therefore, by using Parseval's theorem on Eq. (A8) and using Eq. (A2), we have

$$E^2_{F,k+1} \leq E^2_{Ok} \tag{A17}$$

Combining this with Eq. (A10) gives the desired result

$$E^2_{F,k+1} \leq E^2_{Ok} \leq E^2_{Fk} \tag{A18}$$

That is, the unnormalized mean-squared error must decrease, or at least not increase, with each iteration of the error-reduction approach. The quantities usually considered are the normalized mean-squared errors, Eqs. (4) and

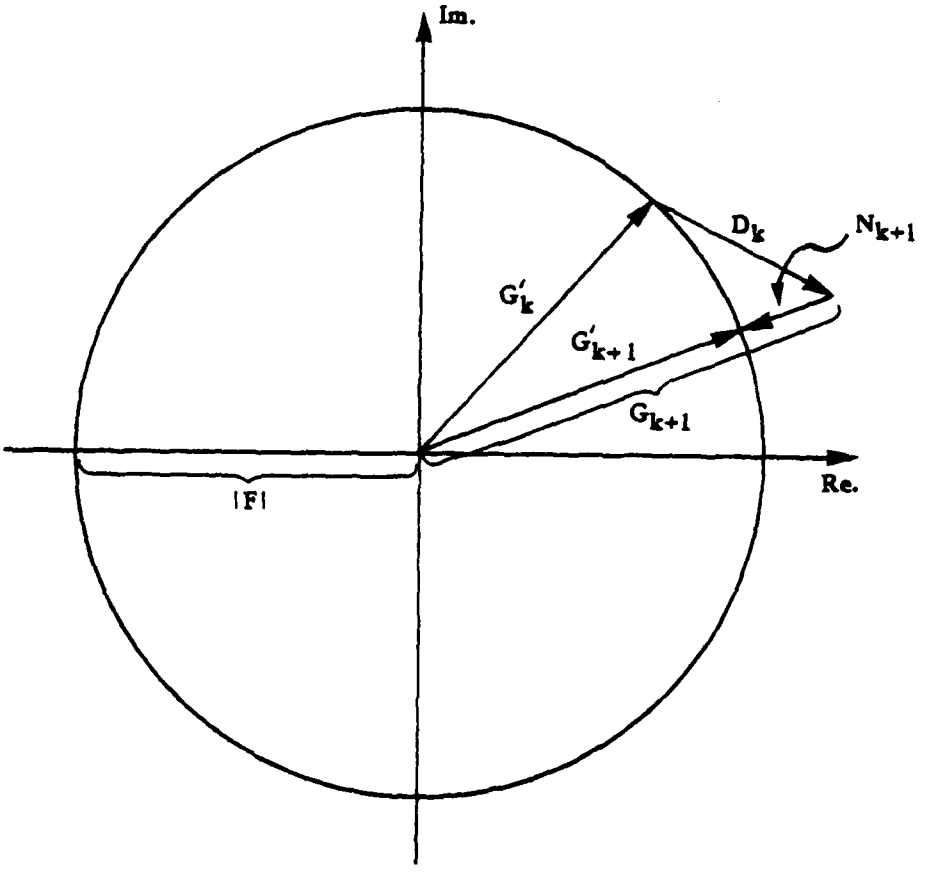

Figure A1. Fourier domain quantities for a given value of (p, q), showing that $|N_{k+1,pq}| \leq |D_{k,pq}|$.

(5). Since these are simply proportional to the unnormalized mean-squared errors, Eq. (A18) also holds for the normalized mean-squared errors.

Complete stagnation of the error reduction approach could occur if $d_{k,mn} = - n_{k,mn}$ for all (m,n), in which case from Eq. (A7) one gets $g_{k+1,mn} = g_{k,mn}$ for all (m,n). Another condition of stagnation is for $\theta_{pq} = 0$ for all (p,q) in Eq. (A15).

REFERENCES

1. A. Labeyrie, "Attainment of Diffraction Limited Resolution in Large Telescopes by Fourier Analyzing Speckle Patterns in Star Images," Astron. and Astrophys. 6, 85-87 (1970); D.Y. Gezari, A. Labeyrie, and R.V. Stachnik, "Speckle Interferometry: Diffraction-Limited Measurements of Nine Stars with the 200-inch Telescope," Astrophys. J. Lett. 173, L1-L5 (1972).

2. J.R. Fienup, "Reconstruction of an Object from the Modulus of Its Fourier Transform," Opt. Lett. 3, 27-29 (1978).

3. J.R. Fienup, "Space Object Imaging Through the Turbulent Atmosphere," Opt. Eng. 18, 529-34, (1979).

4. J.R. Fienup, "Iterative Method Applied to Image Reconstruction and to Computer-Generated Holograms," Opt. Eng. 19, 297-305 (1980).

5. B.L. McGlamery, "Computer Simulation Studies of Compensation of Turbulence Degraded Images," in Proc. of the SPIE 74 Image Processing, pp 225-33 (1976).

6. D.L. Fried, "Optical Resolution Through a Randomly Inhomogeneous Medium for Very Long and Very Short Exposures," J. Opt. Soc. Am. 56, 1372-79 (1962).

7. B.L. McGlamery, "Summary of Procesing for Speckle Simulations," private communication, March 17, 1978.

8. J.W. Goodman and J.F. Belsher, "Fundamental Limitations in Linearly Invariant Restoration of Atmospherically Degraded Images," Proc. of the SPIE 75 Imaging Through the Atmosphere, pp. 141-54 (March 1976).

9. J.C. Dainty and A.H. Greenaway, "Estimation of Spatial Power Spectra in Speckle Interferometry," J. Opt. Soc. Am. 69, 786-90 (1979).

10. J.R. Fienup and G.B. Feldkamp, "Astronomical Imaging by Processing Stellar Speckle Interferometry Data," Proc. of the SPIE 243-16 Applications of Speckle Phenomena, (1980).

11. A. Walther, "The Question of Phase Retrieval in Optics," Optica Acta 10, 41-49 (1963); E.M. Hofstetter, "Construction of Time-Limited Functions with Specified Autocorrelation Functions," IEEE Trans. Info. Theory IT-10, 119-26 (1964).

12. M.A. Fiddy and G. Ross, "Analytic Fourier Optics: the Encoding of Information by Complex Zeroes," Optica Acta 26, 1139-46 (1979).

13. Y.M. Bruck and L.G. Sodin, "On the Ambiguity of the Image Reconstruction Problem," Opt. Commun. 30, 304-08 (1979).

14. W. Lawton, "A Numerical Algorithm for 2-D Wavefront Reconstruction from Intensity Measurements in a Single Plane," in Proc. SPIE 231 Iterative Methods for Reconstructing Images from Incomplete Data, pp. 94-98 (1980).

15. D.L. Fried, "Analysis of Advanced CI Applications and Systems Performance," Interim Report RADC-TR-80-219 (June 1980), Chapter 2.

16. K.T. Knox and B.J. Thompson, "Recovery of Images from Atmospherically Degraded Short-Exposure Photographs," Astrophys. J. Letters 193, L45-L48 (1974).

LME